NPS63-78003

LEVEL

NAVAL POSTGRADUATE SCHOOL
Monterey, California

AN INITIALIZATION PROCEDURE FOR LIMITED-AREA
MODELS FOR NUMERICAL WEATHER PREDICTION

Daniel Keyser

August 1978

Technical Report Period: October 1977-September 1978

78 10 06 015

NAVAL POSTGRADUATE SCHOOL
Monterey, California

Rear Admiral Tyler F. Dedman   Jack R. Borsting
Superintendent   Provost

ABSTRACT

This paper describes a diagnostic objective analysis procedure designed
to derive dynamically consistent three-dimensional fields of horizontal
wind velocity, geopotential and temperature over *limited-area subsynoptic
and mesoscale* domains. These analyses provide data for initial and boundary
conditions for the fine-mesh model tests over the United States and Europe
made at Fleet Numerical Weather Central (FNWC) and described by Anthes
(1978). Objective analyses are produced on nine standard pressure levels
over 70 x 70 unstaggered 60-km Cartesian grids on Lambert conformal map pro-
jections covering the United States and western Europe including the
western Mediterranean Sea.

The analysis procedure utilizes first-guess fields of geopotential,
temperature, relative humidity, geostrophic wind and sea-level pressure
taken from operational analyses on the FNWC northern hemispheric 63 x 63
381-km grid. Wind observations originating from rawinsondes, aircraft,
pilot balloons and satellite-derived cloud motions modify the geostrophic
first-guess wind analyses on pressure surfaces through a successive
correction scheme consisting of two scans using ellipsoidal (three-dimen-
sional) weighting functions. Following the wind analysis, we infer geo-
potential and temperature from the rotational part of the wind with a non-
linear form of the balance equation. This procedure ensures that the wind
and mass fields are consistently related through a simplified set of the
equations of motion.

We present detailed results from two cases and error statistics from
thirty cases occurring from December 1977 through April 1978. Typical
root-mean-square (RMS) differences between first-guess and balanced analyses
of geopotential and temperature are ~20 m and 2°C, while RMS vector differ-
ences between analyzed and balanced winds are ~5 m s^{-1}, a reasonable order
of magnitude for the divergent component of the wind. Discrepancies between
the first-guess and balanced temperature fields, largest near the ground
and at the tropopause, appear to be a consequence of ignoring the divergent
part of the wind when solving for the geopotential and truncation errors
when inferring temperature from geopotential.

Daniel Keyser
Daniel Keyser

Approved by: Released by:

G. J. Haltiner   *William M. Tolles*
G. J. Haltiner, Chairman   William M. Tolles
Department of Meteorology   Dean of Research

1

REPORT DOCUMENTATION PAGE	READ INSTRUCTIONS BEFORE COMPLETING FORM

1. REPORT NUMBER	2. GOVT ACCESSION NO.	3. RECIPIENT'S CATALOG NUMBER
NPS-63-78003		

4. TITLE (and Subtitle)	5. TYPE OF REPORT & PERIOD COVERED
An Initialization Procedure for Limited-Area Models for Numerical Weather Prediction	Final rept. October 1977–September 1978
	6. PERFORMING ORG. REPORT NUMBER

7. AUTHOR(s)	8. CONTRACT OR GRANT NUMBER(s)
Daniel Keyser	

9. PERFORMING ORGANIZATION NAME AND ADDRESS	10. PROGRAM ELEMENT, PROJECT, TASK AREA & WORK UNIT NUMBERS
Naval Postgraduate School Monterey, California 93940	61153N, N 00019-78-WR-81002

11. CONTROLLING OFFICE NAME AND ADDRESS	12. REPORT DATE
Foundation Research Program of the Naval Postgraduate School	August 1978
	13. NUMBER OF PAGES
	72

14. MONITORING AGENCY NAME & ADDRESS(if different from Controlling Office)	15. SECURITY CLASS. (of this report)
73 p.	Unclassified
	15a. DECLASSIFICATION/DOWNGRADING SCHEDULE

16. DISTRIBUTION STATEMENT (of this Report)

Approved for public release; distribution unlimited.

17. DISTRIBUTION STATEMENT (of the abstract entered in Block 20, if different from Report)

18. SUPPLEMENTARY NOTES

19. KEY WORDS (Continue on reverse side if necessary and identify by block number)

Initialization	Balance equation
Limited-area model	Objective wind analysis

20. ABSTRACT (Continue on reverse side if necessary and identify by block number)

This paper describes a diagnostic objective analysis procedure designed to derive dynamically consistent three-dimensional fields of horizontal wind velocity, geopotential and temperature over limited-area subsynoptic and mesoscale domains. These analyses provide data for initial and boundary conditions for the fine-mesh model tests over the United States and Europe made at Fleet Numerical Weather Central (FNWC) and described by Anthes (1978).

DD FORM 1473 EDITION OF 1 NOV 65 IS OBSOLETE
1 JAN 73
S/N 0102-014-6601

2

251 450

Objective analyses are produced on nine standard pressure levels over 70 x 70 unstaggered 60-km Cartesian grids on Lambert conformal map projections covering the United States and western Europe including the western Mediterranean Sea.

The analysis procedure utilizes first-guess fields of geopotential, temperature, relative humidity, geostrophic wind and sea-level pressure taken from operational analyses on the FNWC northern hemispheric 63 x 63 381-km grid. Wind observations originating from rawinsondes, aircraft, pilot balloons and satellite-derived cloud motions modify the geostrophic first-guess wind analyses on pressure surfaces through a successive correction scheme consisting of two scans using ellipsoidal (three-dimensional) weighting functions. Following the wind analysis, we infer geopotential and temperature from the rotational part of the wind with a nonlinear form of the balance equation. This procedure ensures that the wind and mass fields are consistently related through a simplified set of the equations of motion.

We present detailed results from two cases and error statistics from thirty cases occurring from December 1977 through April 1978. Typical root-mean-square (RMS) differences between first-guess and balanced analyses of geopotential and temperature are ~20 m and 2°C, while RMS vector differences between analyzed and balanced winds are ~5 m s^{-1}, a reasonable order of magnitude for the divergent component of the wind. Discrepancies between the first-guess and balanced temperature fields, largest near the ground and at the tropopause, appear to be a consequence of ignoring the divergent part of the wind when solving for the geopotential and truncation errors when inferring temperature from geopotential.

ACCESSION for

NTIS   White Section

DDC   Buff Section

UNANNOUNCED

JUSTIFICATION

BY

DISTRIBUTION/AVAILABILITY CODES

Dist   SPECIAL

A

1. Introduction

The development and implementation of operational numerical weather prediction models have required the concomitant application of objective analysis schemes to provide data for initial conditions and verification, and, in the case of limited-area models in a research mode, time-dependent boundary conditions. The initial conditions for a primitive equation model not only should reproduce the features in the flow within the scales of motion resolvable by the model, but should imply local time tendencies of the dependent variables characteristic of the analyzed features. Failure to satisfy the latter requirement leads to gravity-wave noise early in the forecast.

Independent analyses of the wind and mass (specified by the surface pressure and three-dimensional temperature patterns) invariably lead to gravity-wave generation in models because these fields are mutually related through the equations of motion. Therefore, however carefully one prepares independent analyses of the wind and mass field, small inconsistencies between these fields will result in spurious initial accelerations typical of gravity waves. The traditional technique for obtaining mutually consistent initial analyses for mid-latitude synoptic-scale models has been to derive the wind field from the mass field through a diagnostic relationship such as the geostrophic wind law or a diagnostic form of the divergence equation known as the balance equation.

This paper explores the feasibility of utilizing the reverse procedure of inferring the mass field from the wind field, which is standard procedure in tropical regions, for meso- and subsynoptic-scale motions in mid-latitudes. Given analyses of sea-level pressure, boundary geopotential, and the rotational part of the wind, we derive interior geopotential and temperature

4

using the nonlinear balance equation. The scheme was tested in 15 cases over North America and 15 cases over Europe and North Africa from December 1977 through April 1978. Furthermore, the same analysis procedure generated initial and boundary data for the version of The Pennsylvania State University mesoscale model (Anthes and Warner, 1978) tested at the Naval Environmental Prediction Research Facility (NEPRF) and Fleet Numerical Weather Central (FNWC) in early 1978. The results of thirty-two forecasts over the eastern two-thirds of the United States and western Europe, including the western Mediterranean Sea, are given in a separate report (Anthes, 1978).

2. Analysis procedure

The analysis procedure comprises three main steps: obtaining first-guess fields of geopotential, temperature, relative humidity and horizontal wind velocity; producing a mesoscale analysis of the rotational part of the observed winds; and inferring geopotential and temperature from the nonlinear balance equation.

The analyses are prepared on 70 x 70 60-km unstaggered Cartesian grids on Lambert conformal map projections for Europe and North Africa (grid centered at 45°N, 5°E) and North America (grid centered 40°N, 90°W). Figs. 1a and 1b show the geographical extent of the domains. The interior region of the 70 x 70 grids, delineated by the inner box, marks the 50 x 50 60-km model forecast domain. We perform the analyses on the larger domain to minimize the effect of boundary wind errors on the model initial conditions (Elsberry and Ley, 1976). This rationale is justified in the Appendix.

a. Determination of the first-guess fields

We obtain first-guess fields of sea-level pressure, geopotential, temperature, and vapor pressure (which is immediately converted to relative humidity) on a rectangular subsection of the FNWC 63 x 63 381-km northern
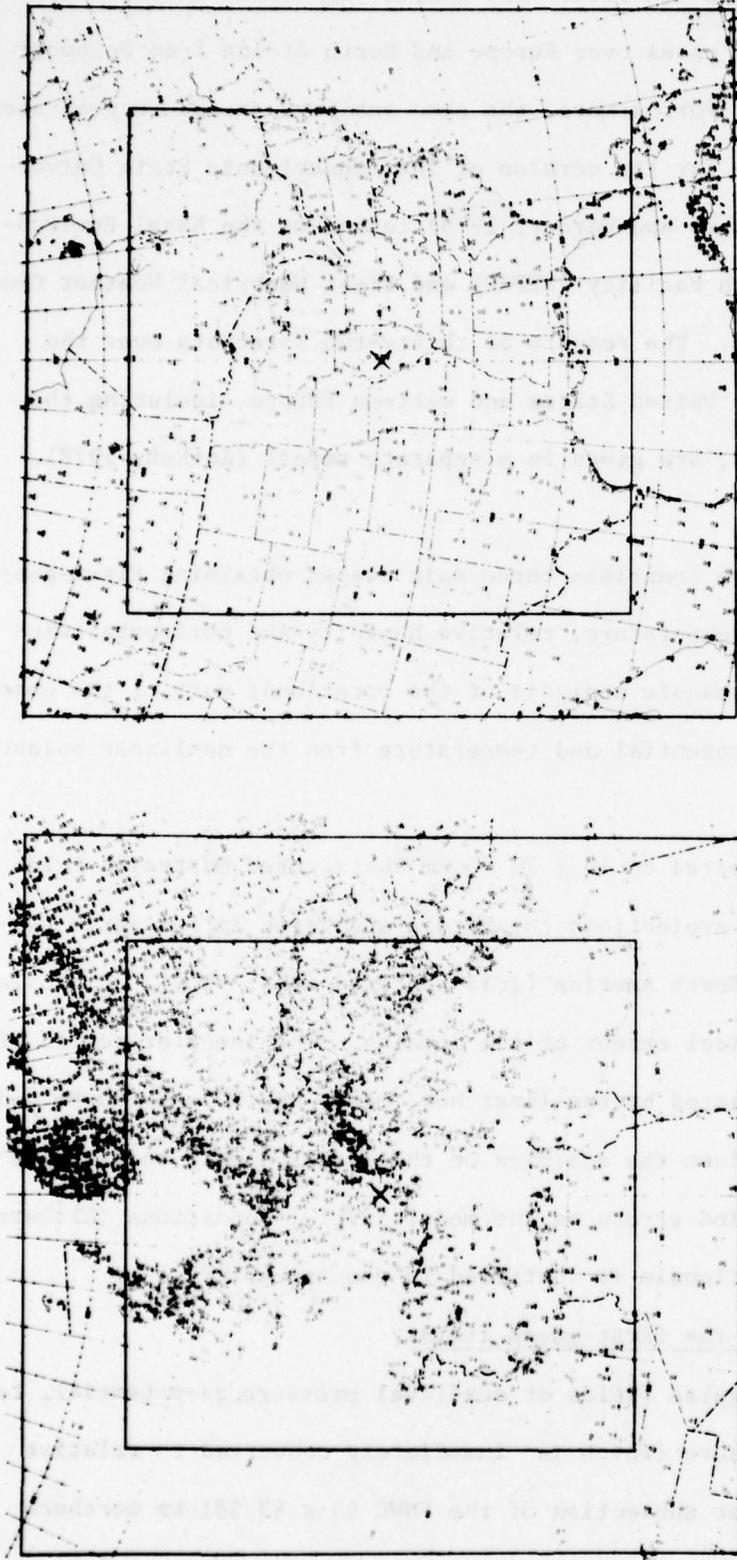
5

Figure 1. Charts showing domains used in this study. Outer box marks boundaries of 70 x 70 60-km analysis domain; inner box marks boundaries of 50 x 50 60-km model forecast domain. Center points are marked with an "X".

a. European domain

b. United States domain

6

hemispheric polar stereographic grid that includes the 70 x 70 analysis domain. Geopotential and temperature are taken from analyses at 925, 850, 700, 500, 400, 300, 250, 200, 150 and 100 mb; vapor pressure is obtained from a 12-h forecast of the FNWC operational model (Kesel and Winninghoff, 1972) valid at the analysis time at the same pressure levels at and below 300 mb. After computing geostrophic winds on the FNWC subset grid at all pressure levels, we interpolate all the fields to the 70 x 70 analysis domain using cubic splines under tension (Cline, 1974) with the tension factor equal to one. Although the first-guess moisture analysis does not contain mesoscale details, we leave it unmodified during the remainder of the analysis procedure and neglect its effects on the mass and wind fields. Nevertheless, the need for a detailed, high-resolution moisture analysis for initializing mesoscale models justifies additional attention to this problem. Finally, we note that the procedure for obtaining the first-guess fields requires about 100 s of execution (CP) time on FNWC's CDC CYBER-175 computer.

b. Analysis of observed winds

After obtaining the first-guess analyses on the 70 x 70 analysis grid, we perform a three-dimensional objective analysis of observed winds on pressure levels using a procedure developed by Barker at NEPRF (personal communication). The scheme consists of modifying the geostrophic first-guess analyses by performing two scans with ellipsoidal (three-dimensional) weighting functions, which allows one to specify the minimum scales in the final wind analysis ($\sim$240 km = $4\Delta s$ in this case).

Wind observations originate from rawinsondes, aircraft, pilot balloons, and satellite-observed cloud motions. The wind observations are not corrected for balloon drift or observation time differing slightly from the analysis time. Finally, the wind analysis scheme is coded so that a horizontal vector

7

wind observation is contained within one word of memory, so it can be treated computationally as a scalar. For ten pressure levels on the 70 x 70 domain, the wind analysis requires about 120 s of execution time.

c. Solution for the mass field

Given detailed wind analyses and boundary geopotential on the 70 x 70 analysis domain, we derive the interior geopotential and temperature fields with the nonlinear balance equation and the hydrostatic assumption.

We choose to deviate from standard mid-latitude practice of inferring wind from mass (Shuman, 1957) because the noise in the observed height field (~10 m) implies an unacceptable noise level in the geostrophic wind of 16.3 m s^{-1} for a 60-km grid spacing and the Coriolis parameter $f = 10^{-4}$ s^{-1}. The same problem occurs in tropical analysis of synoptic-scale motions where a decrease in f compensates for the increased grid spacing. Therefore, despite the risk of incurring errors from uncertainties in wind observations, especially in situations where winds are strong and at high levels, causing low elevation angles of pilot balloons or rawinsondes, we favor inferring mass from the winds (Fankhauser, 1974; Anthes, 1976).

Considerations of a mathematical nature provide an additional argument for starting with the winds. The usual procedure of solving the nonlinear balance equation (see (12)) for the stream function from geopotential requires solution of an elliptic partial differential equation, which has unique solutions provided that

$$\zeta_g > -\frac{f}{2}, \tag{1}$$

where ζ_g is the relative geostrophic vorticity on a pressure surface (Haltiner, 1971). While the constraint in (1) is usually not critical in synoptic-scale analyses, it does not permit realistic mesoscale resolution of anticyclonic

8

shear zones, especially those associated with jet streaks. The alternative of deriving mass from wind, however, only requires solution of a Poisson equation, which is always elliptic and solvable by a straightforward procedure.

The first stage of the balancing procedure consists of deriving the stream function from the rotational part of the observed wind. According to Helmholtz's theorem, the rotational part of the wind

$$\underset{\sim}{V}_\psi = \hat{k} \times m\nabla\psi \,, \tag{2}$$

where ψ is the nondivergent stream function, $\hat{k}$ the vertical unit vector, m the map-scale factor, and $\nabla = \hat{i} \dfrac{\partial}{\partial x_p} + \hat{j} \dfrac{\partial}{\partial y_p}$.

From (2), the component of the wind normal to the boundary is

$$v_n = -m \frac{\partial\psi}{\partial s} \,, \tag{3}$$

where s is distance along the boundary, positive when taken counterclockwise. Following Phillips (1958), Brown and Neilon (1961), Bedient and Vederman (1964), Anthes (1976), we compute the boundary stream function, ψ_B, by adding a correction factor (constant for each pressure level) that forces the mean observed velocity component normal to the boundary, v_n^{obs}, to be zero. Formally, we write

$$v_n = v_n^{obs} + c \,, \tag{4}$$

where

$$\oint \frac{v_n}{m} ds = \oint \left(\frac{v_n^{obs}}{m} + \frac{c}{m}\right) ds = 0 \,, \tag{5}$$

so that

$$c = -\frac{\oint \dfrac{v_n^{obs}}{m} ds}{\oint \dfrac{ds}{m}} \,. \tag{6}$$

9

The magnitude of the correction factor, c, is usually less than 1 m s^{-1} for the domains we consider. From (3), (4) and (6), we conclude that

$$\psi_B(s) = \psi_B(s_o) - \int_{s_o}^{s} \frac{v_n}{m} \, ds \, , \qquad (7)$$

where s_o applies at the southwest corner of the domain.

Given $\psi_B(s)$ from (7), we determine ψ in the domain interior by solving the Poisson equation implied by (2)

$$\nabla^2 \psi = \frac{\zeta^{obs}}{m^2} \, , \qquad (8)$$

where

$$\zeta^{obs} = m^2 \left[\frac{\partial}{\partial x} \left(\frac{v^{obs}}{m} \right) - \frac{\partial}{\partial y} \left(\frac{u^{obs}}{m} \right) \right] \, . \qquad (9)$$

Eq. (8) is approximated by centered-in-space differences on an unstaggered grid and solved with an efficient direct method (Rosmond and Faulkner, 1976). In finite-difference form the Laplacian operator is

$$\nabla^2 \psi \approx (\psi_{ij+1} + \psi_{i-1j} + \psi_{ij-1} + \psi_{i+1j} - 4\psi_{ij})/(\Delta s)^2 \, , \qquad (10)$$

where i and j are indices in the y and x directions, respectively. One can show, however, from the finite difference form of the vorticity (9) that

$$\nabla^2 \psi \approx (\psi_{ij+2} + \psi_{i-2j} + \psi_{ij-2} + \psi_{i+2j} - 4\psi_{ij})/(2\Delta s)^2 \qquad (11)$$

is actually the consistent form ensuring that the vorticity of the balanced wind equals that of the observed wind. We choose (10) in order to avoid needing two sets of boundary conditions while noting that both (10) and (11) yield nondivergent winds.

10

The second stage of the balancing procedure consists of solving the nonlinear balance equation

$$\nabla^2 \phi = \nabla \cdot (f \nabla \psi) + 2m^2 J(\frac{\partial \psi}{\partial x} , \frac{\partial \psi}{\partial y}) \qquad (12)$$

for geopotential, ϕ. In (12), J is the Jacobian operator, and we include the full variation of f, which for the Lambert conformal projection varies in x as well as y. In addition, we have neglected the spatial variation of the map-scale factor. Eq. (12) is consistent with neglecting the horizontal velocity divergence D, dD/dt, and friction in the full divergence equation.

The right side of (12) is known, so that it can be solved by the same technique used for (8) with the first-guess ϕ fields interpolated to the boundaries of the 70 x 70 grid serving as boundary conditions. As discussed in the Appendix, the lack of mesoscale detail in ϕ on the boundaries is acceptable, since for a given amplitude the exponential damping of the influence of a boundary harmonic with distance into the domain interior is faster for higher wavenumbers. Accurately specifying the large-scale variation of ϕ on the boundaries is important, and we believe the FNWC analysis is sufficiently reliable for this purpose.

After solving (12), our analysis will be complete once the temperature is determined. Using the hydrostatic assumption on the derived geopotentials and first-guess sea-level pressure fields, we determine estimates of temperatures at intermediate levels determined by the logarithmic mean pressure between the analysis levels. Then the temperatures are interpolated linearly with respect to the natural logarithm of pressure to the analysis levels. The balancing procedure requires about 20 s of execution time compared to a total of 240 s for the entire analysis procedure.

11

3. Examples of the analysis procedure

In order to illustrate the analysis procedure, we examine 300-mb winds and 500-mb heights and temperatures for the 50 x 50 model forecast domains over western Europe (Fig. 1a) and the United States (Fig. 1b) for 0000 GMT 12 January 1978 and 1200 GMT 25 January 1978, respectively. The forecasts based on these initial conditions are discussed by Anthes (1978). Because these cases feature large height and temperature gradients, strong winds and pronounced streamline curvature, they are atypical of situations commonly encountered, and thus provide a stringent test of the assumptions in the balancing procedure.

a. European case of 0000 GMT 12 January 1978

Fig. 2 shows the sea-level pressure pattern over western Europe that foreshadowed cyclogenesis in the Gulf of Genoa. An old occluded low (992 mb) over the Netherlands is weakening and a low is developing in the Mediterranean Sea south of France. We mention that the sea-level pressure pattern does not exhibit mesoscale detail because it is the unmodified first-guess interpolated from the FNWC hemispheric analysis.

The 500-mb temperatures and D values (h-5574m) for the first-guess and balanced cases for 0000 GMT 12 January 1978 are displayed in Figs. 3a and 3b, respectively. The temperatures and D values do not match on the boundaries because only the 50 x 50 interior points of the 70 x 70 analysis domain are shown. Both analyses show a high-amplitude, tilted short-wave trough in the height fields with a diffluent region over the area of incipient cyclogenesis. The balanced analysis contains a cutoff low above the occluding surface system, while the FNWC first-guess analysis shows a sharp trough.

The first-guess temperature analysis (Fig. 3a) contains a cold dome (~ -35°C) centered over the Bay of Biscay and a mid-tropospheric frontal zone at the base of the trough in the height field. The balanced analysis (Fig. 3b)
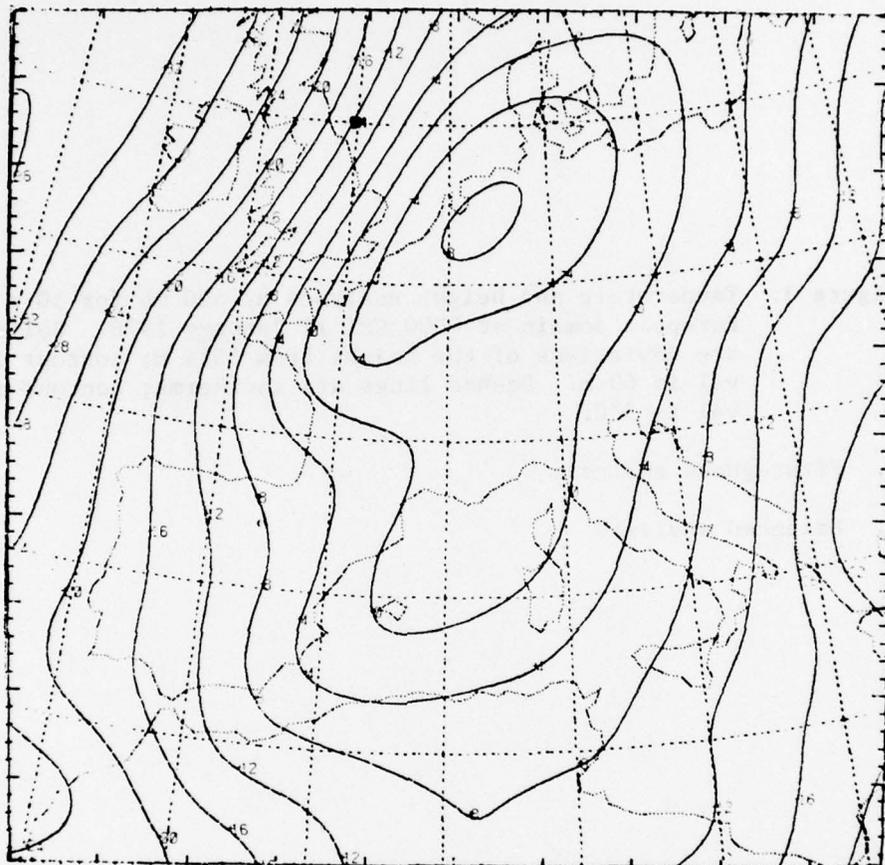
12

Figure 2.   First-guess sea-level pressure analysis for 50 x 50
European domain at 0000 GMT 12 January 1978.   Solid
lines are deviations of sea-level pressure from
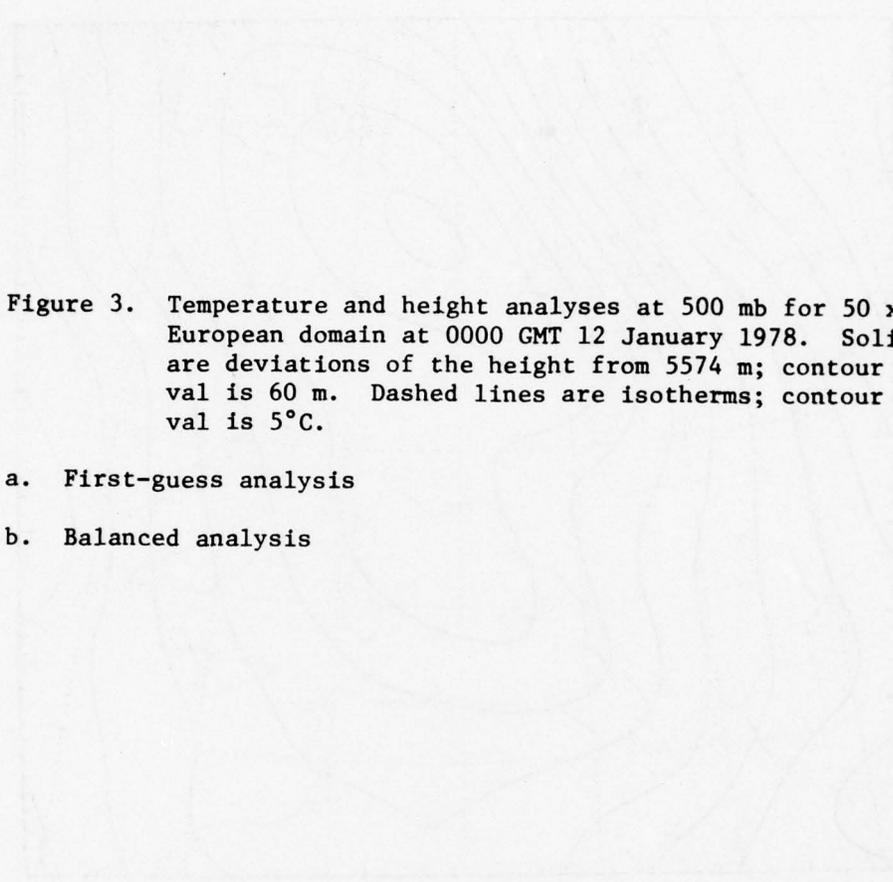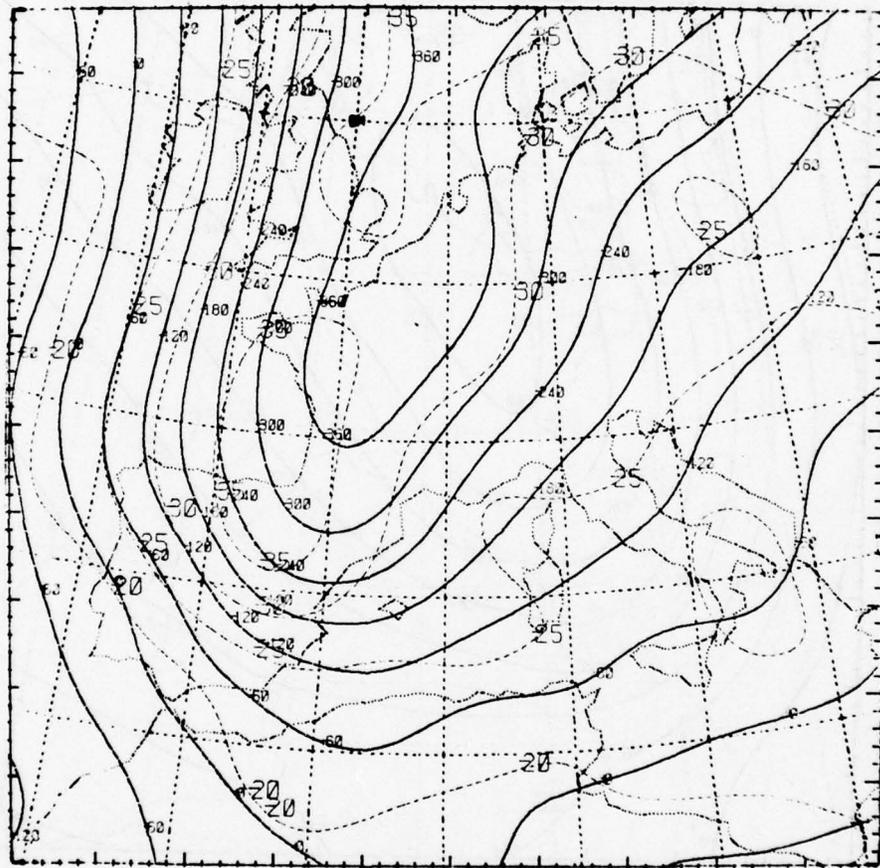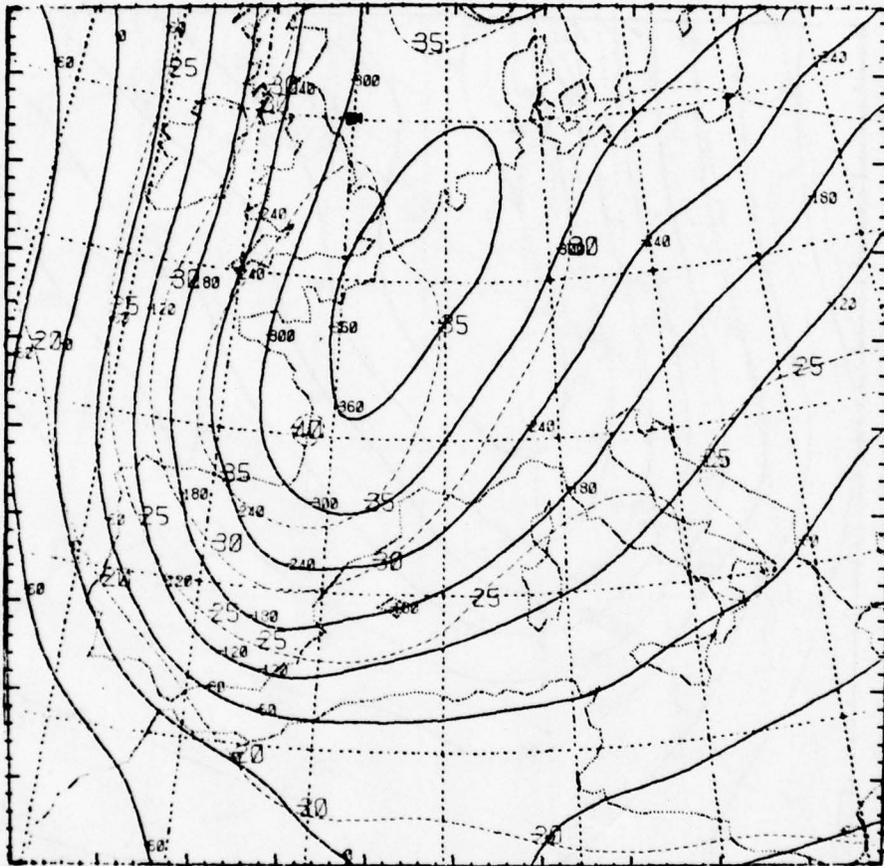1000 mb; contour interval is 4 mb.

Figure 3.   Temperature and height analyses at 500 mb for 50 x 50
            European domain at 0000 GMT 12 January 1978.   Solid lines
            are deviations of the height from 5574 m; contour inter-
            val is 60 m.   Dashed lines are isotherms; contour inter-
            val is 5°C.

a.   First-guess analysis

b.   Balanced analysis

(3a)

(3b)

16

has relaxed the temperature gradient in the frontal zone and produced a small minimum of -40°C over the west coast of France, which is about -5°C lower than in the first-guess analysis. The smoothing of the frontal zone can be explained by recalling that temperatures are computed hydrostatically over layers ~100 mb thick, while typical mid-tropospheric frontal zones are 50-100 mb deep. Therefore, the region of high static stability marking the frontal zone is smoothed vertically, and, in order to preserve the frontal slope and thermal wind balance, horizontal smoothing results as well. The bias towards low balanced temperatures in cyclonically curved systems is not confined to this case and will be explained later.

Wind analyses at 300 mb, approximately the level of maximum wind, are shown in Figs. 4a, 4b and 4c. Fig. 4a displays the result of interpolating geostrophic winds computed on the FNWC 381-km grid to the 60-km analysis grid. A cyclonically curved jet streak appears on the west side of the trough, a broad southwesterly stream of air covers central Europe, and a weak short-wave in the wind pattern is located over Italy.

The observed wind analysis (Fig. 4b), while reflecting the first-guess flow pattern, is far more detailed. In particular, the 70-m s^{-1} jet maximum over the northwestern corner of Spain is 10 m s^{-1} stronger, but of smaller-scale and less elongated. Removing the observed divergence from the wind (Fig. 4c) eliminates much of the small-scale detail, confirming the hypothesis that the magnitude of the observed divergent part of the wind lies within the noise level of the observations and their subsequent analysis. In the nondivergent analysis (Fig. 4c), the jet streak is weaker than in the observed wind analysis (65 m s^{-1} compared to 75 m s^{-1}) and the isotachs are more elliptical. Comparing the nondivergent analysis (Fig. 4c) with the first-guess analysis (Fig. 4a) shows the cross-jet width to be less in the former. In particular, we note

17

Figure 4. Wind analyses at 300 mb for 50 x 50 European domain at 0000 GMT 12 January 1978. Solid lines are isotachs; contour interval is 10 m s^{-1}. On wind arrows, flags, full barbs and half barbs denote speeds of 50, 10 and 5 m s^{-1}, respectively.

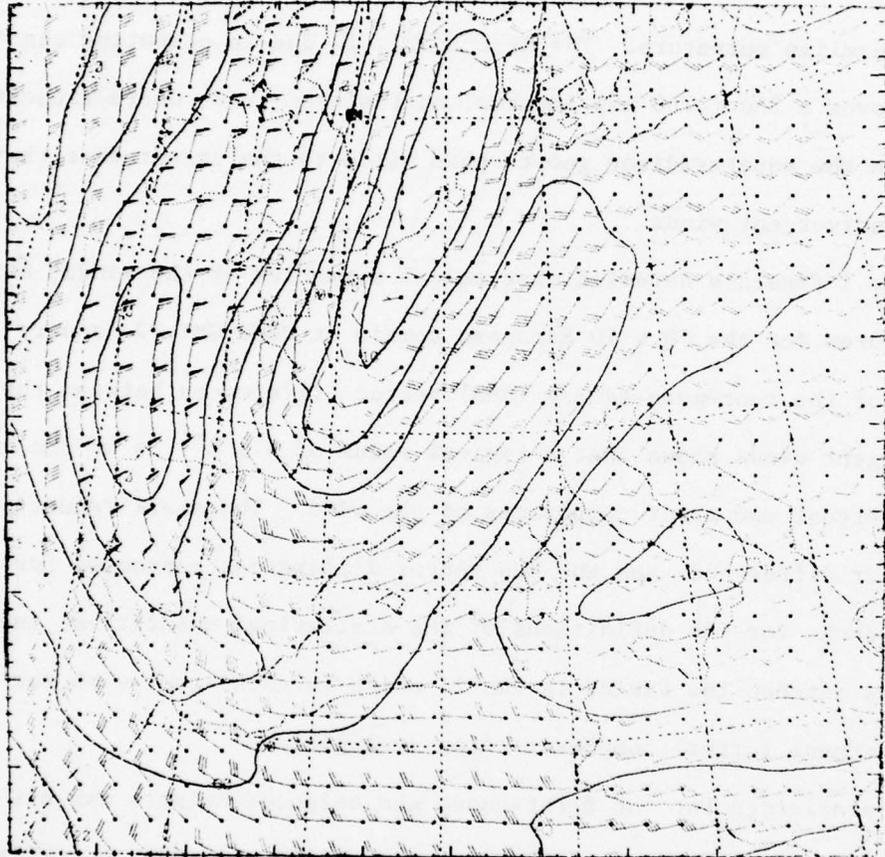a. First-guess wind analysis

b. Objective analysis of observed winds

c. Nondivergent wind analysis
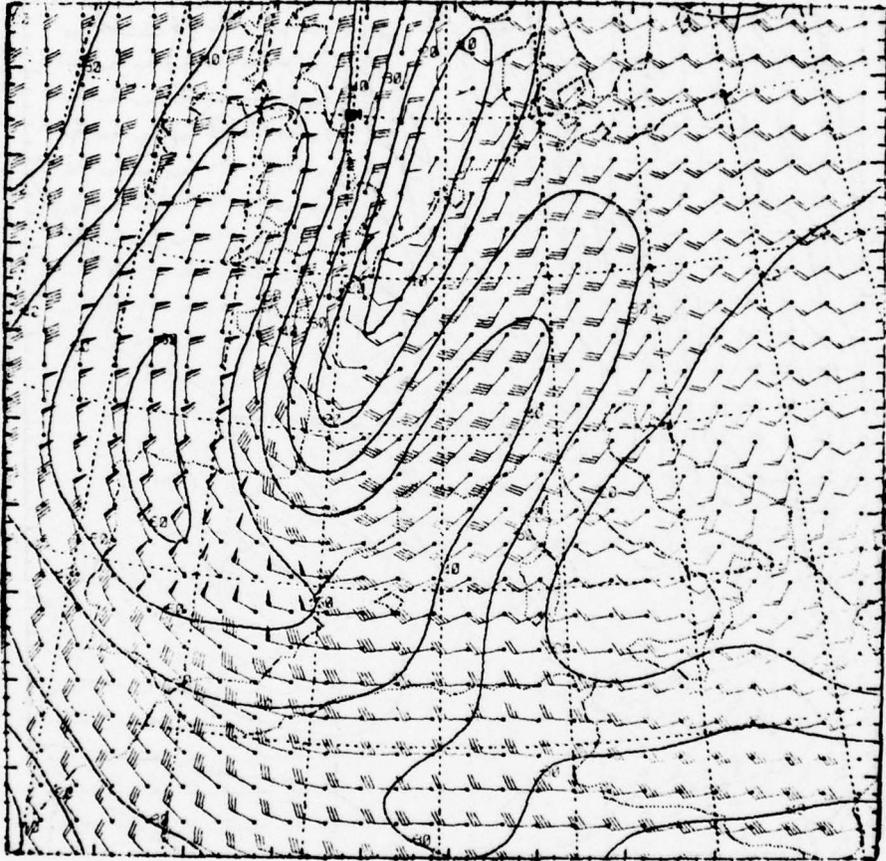
(4a)
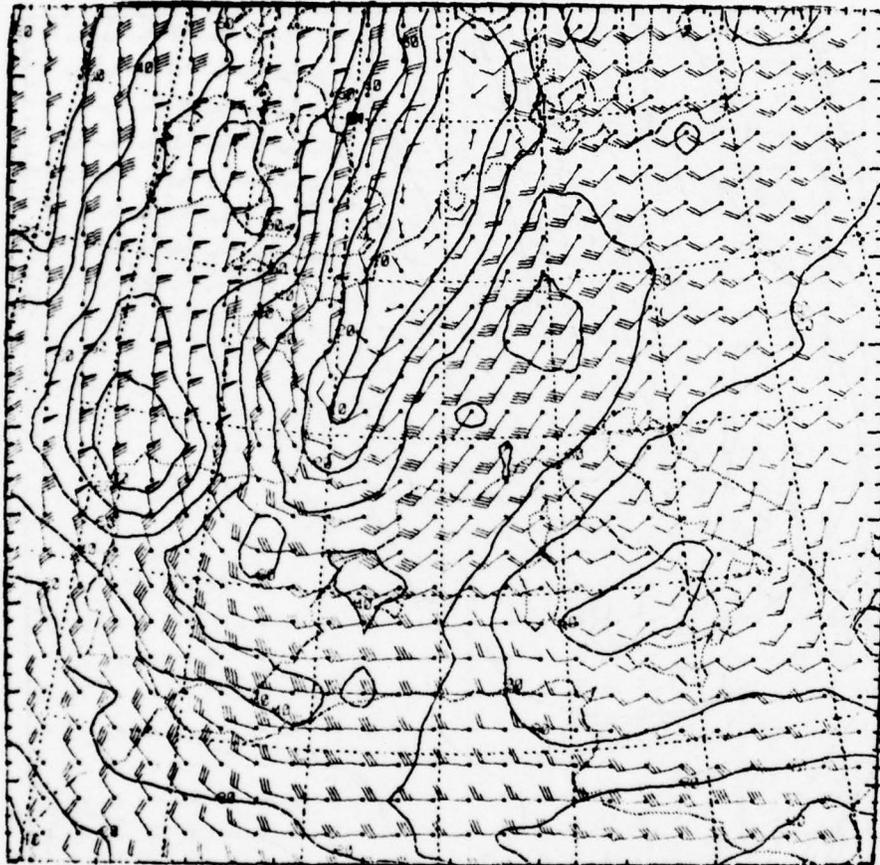
(4b)

(4c)

that the area covered by the 50 m s^{-1} isotach is narrower. In addition to rendering a more realistic jet streak than that in the first-guess analysis, the nondivergent wind analysis preserves the short wave over Italy.

One may question why the differences in wind speeds in the trough between the first-guess and balanced analysis are not greater in view of the large cyclonic streamline curvature. The discrepancy is due to computing the first-guess winds over a 2Δs (~760 km) interval on the FNWC grid, where truncation errors weaken the supergradient geostrophic winds to the extent that they roughly equal the nondivergent winds.

Table 1 presents detailed statistical summaries of the winds, heights and temperatures for the 70 x 70 European domain at 0000 GMT 12 January 1978. Examination of the root-mean-square (RMS) vector differences between the observed and nondivergent winds shows that a typical value of 3 m s^{-1} is on the order of both the divergent and error components of the wind. The small reduction between the RMS vector differences and the RMS vector differences corrected for the mean (see the Appendix for the definitions of the statistical quantities) indicates that the bias between the fields is small, which is consistent with the domain-averaged divergent (error) component being negligible.

The statistics for the first-guess and balanced heights exhibit RMS differences ranging from 6 m at 925 mb to 22 m at 100 mb. When normalized by the geometric mean of the standard deviations of the first-guess and balanced heights, the RMS errors are seen to increase in proportion to the increasing variance in the height fields with elevation. The magnitude of the RMS height differences are comparable to the 10-m errors Fankhauser (1974) quoted for the solution of the complete divergence equation for geopotential on a mesoscale grid with 10-km spacing. The temperature statistics indicate that the discrepancies between the first-guess and balanced analyses are largest near the ground

22

Table 1. Statistical summaries for first-guess, fg, and balanced, b, winds, V; heights, h; and temperatures, T; for European domain ãt 0000 GMT 12 January 1978. Statistical quantities are defined in the Appendix.

p (mb)	$\bar{u}_{fg}$	$\bar{v}_{fg}$	$s(V_{\sim fg})$ (m s^{-1})	$\bar{u}_b$	$\bar{v}_b$	$s(V_{\sim b})$	RMSD($V_{\sim fg,b}$)	RMSDC($V_{\sim fg,b}$)
925	1.67	-1.02	12.69	0.77	-0.84	12.75	2.35	2.17
850	2.71	-1.28	12.57	1.85	-1.17	12.60	2.41	2.25
700	4.96	-2.08	13.37	4.12	-2.15	13.35	2.45	2.30
500	8.82	-3.92	17.77	8.29	-3.99	17.64	2.65	2.59
400	12.02	-5.27	22.04	11.58	-5.23	21.81	3.00	2.97
300	16.83	-6.77	26.28	16.23	-6.63	26.06	3.40	3.35
250	19.26	-7.62	27.13	18.68	-7.53	27.00	3.34	3.29
200	21.20	-8.12	26.98	20.77	-8.16	26.93	3.30	3.27
150	22.28	-6.92	24.47	22.13	-6.82	24.34	3.54	3.53
100	22.15	-5.54	19.80	21.90	-4.72	19.60	3.38	3.27

p (mb)	$\bar{h}_{fg}$	$s(h_{fg})$	$\bar{h}_b$ (m)	$s(h_b)$	$\bar{h}_b - \bar{h}_{fg}$	RMSD($h_{fg,b}$)	RMSDC($h_{fg,b}$)	$s(h_{fg,b})$
925	764.67	91.05	762.92	88.99	-1.75	6.38	6.14	0.071
850	1444.76	94.45	1443.32	92.65	-1.44	6.81	6.65	0.073
700	2972.58	113.84	2970.02	112.09	-2.56	8.79	8.40	0.078
500	5503.61	171.55	5498.09	171.09	-5.52	13.25	12.04	0.077
400	7094.12	212.26	7086.88	215.07	-7.24	15.71	13.95	0.074
300	9039.23	258.93	9032.84	263.22	-6.39	16.54	15.26	0.063
250	10217.75	278.78	10212.86	281.51	-4.89	14.15	13.28	0.051
200	11621.34	288.85	11618.69	288.86	-2.65	15.84	15.61	0.055
150	13412.12	287.95	13409.88	283.40	-2.24	22.06	21.94	0.077
100	15926.47	285.13	15925.47	277.69	-1.00	22.26	22.23	0.079

23

Table 1. (concluded)

p (mb)	$\bar{T}_{fg}$	$s(T_{fg})$ (K)	$\bar{T}_b$	$s(T_b)$	$\bar{T}_b - \bar{T}_{fg}$	$RMSD(T_{fg,b})$	$RMSDC(T_{fg,b})$	$s(T_{fg,b})$
925	276.01	6.16	276.09	6.28	0.08	1.67	1.66	0.269
850	272.25	5.87	272.79	5.68	0.54	1.15	1.02	0.199
700	264.43	6.19	263.97	5.97	−0.46	1.05	0.95	0.173
500	248.85	6.90	248.30	6.86	−0.55	1.30	1.18	0.189
400	237.68	6.81	237.66	6.62	−0.02	1.06	1.06	0.158
300	224.01	6.16	224.75	5.32	0.74	1.72	1.55	0.300
250	216.66	5.07	218.28	4.34	1.62	2.23	1.53	0.475
200	212.52	4.98	213.97	3.50	1.45	2.69	2.26	0.644
150	212.49	4.70	212.25	4.06	−0.24	1.39	1.37	0.318

and tropopause, while the closest agreement is in the middle troposphere.

b. United States case of 1200 GMT 25 January 1978

Although qualitative differences between first-guess, observed and balanced analyses are quite similar in this case to those in the preceding European case, we include it because the synoptic situation developed into the worst blizzard on record in the Ohio Valley with a central pressure of 958 mb at Cleveland at 1200 GMT 26 January 1978 and hurricane-force winds near the storm center (Wagner, 1978). Anthes (1978) discusses the model forecast based on the initial conditions given in this section.

The first-guess sea-level pressure pattern (Fig. 5) exhibits low pressure centers in northern Minnesota and the Gulf States. Comparison with the National Meteorological Center's (NMC) hand-analyzed sea-level pressure chart (not shown) reveals that although the pressure gradients are resolved reasonably well, the central pressures of the lows (1000 mb and 998 mb for the northern and southern systems, respectively) are several millibars too high as expected for a large-scale analysis.

The first-guess and balanced 500-mb charts (Figs. 6a and 6b) show a vigorous short-wave trough over Oklahoma and Texas "phasing" with a cutoff low over eastern North Dakota. The balanced D values for the central height in this low are about 60 m higher than in the FNWC first-guess analysis. The same holds for the Oklahoma-Texas trough. As with the European case, the cold bias appears in the balanced analysis in regions of cyclonic curvature, while in straight flow the agreement is closer as revealed by the relative positions of the -20°C isotherms in the eastern United States (compare Figs. 6a and 6b). Finally, we mention that the 500-mb first-guess temperatures and D-values agree very closely with the NMC analysis and observations (not shown), so for verification purposes, we will consider the first-guess height and temperature analyses as the true mass field.

25
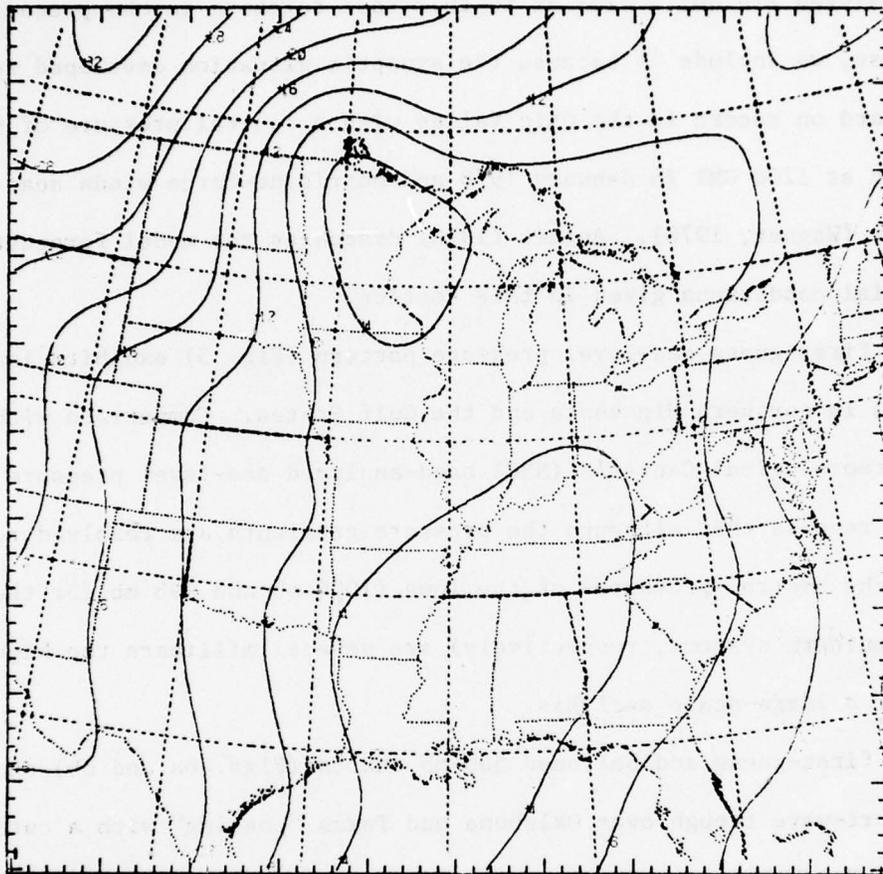
Figure 5.　First-guess sea-level pressure analysis for 50 x 50
United States domain at 1200 GMT 25 January 1978.
Solid lines are deviations of sea-level pressure from
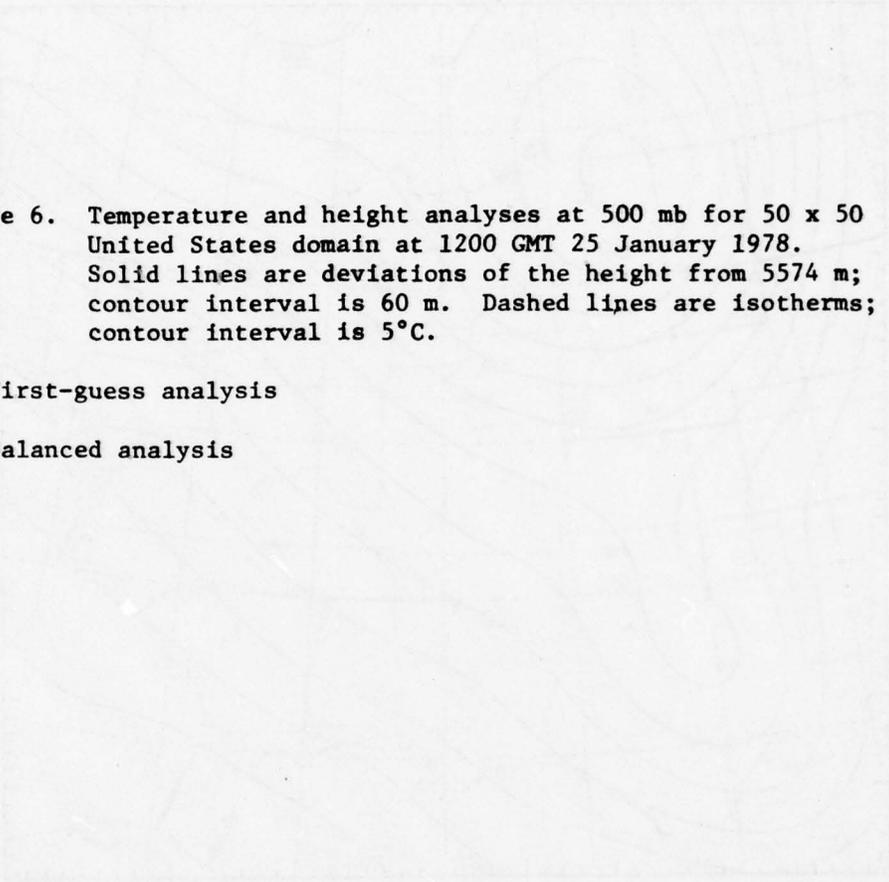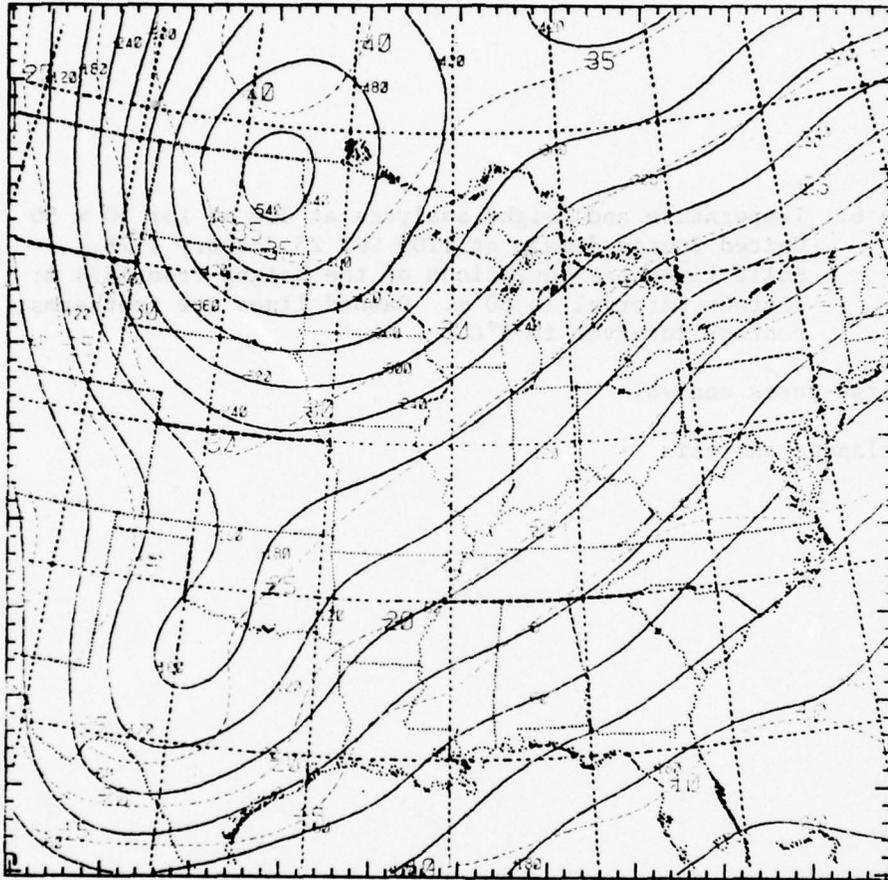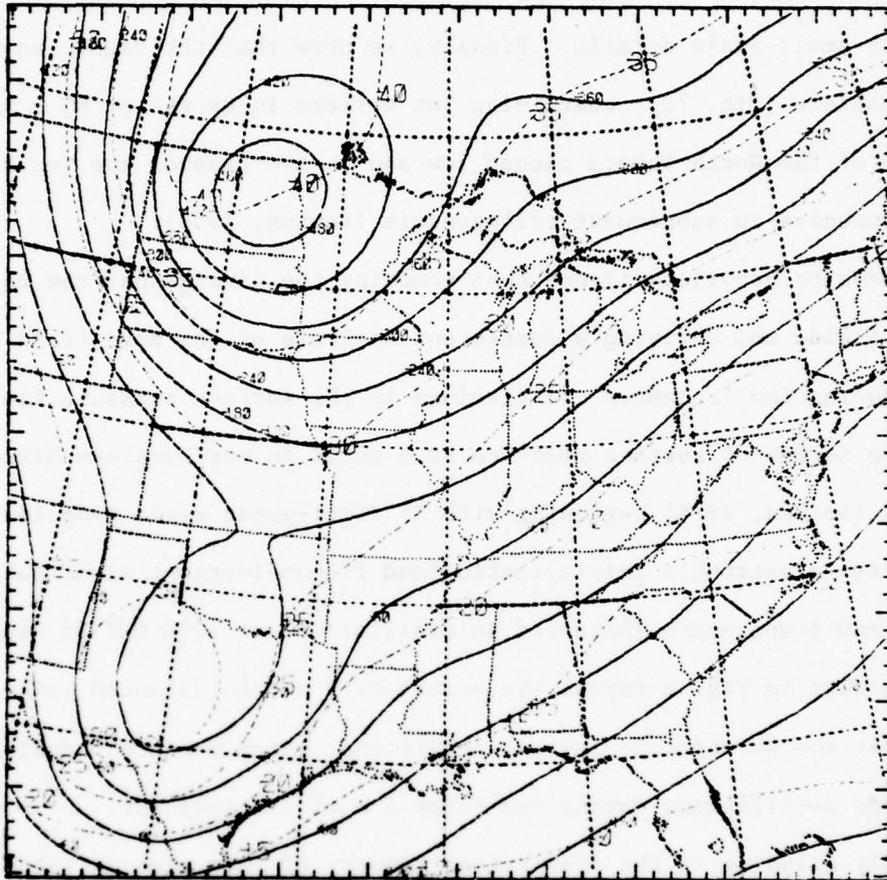1000 mb; contour interval is 4 mb.

Figure 6.   Temperature and height analyses at 500 mb for 50 x 50
            United States domain at 1200 GMT 25 January 1978.
            Solid lines are deviations of the height from 5574 m;
            contour interval is 60 m.   Dashed lines are isotherms;
            contour interval is 5°C.

a.   First-guess analysis

b.   Balanced analysis

(6a)

(6b)

29

The 300-mb first-guess, observed and nondivergent wind analyses display characteristics similar to their European counterparts. Overall, the nondivergent wind analysis (Fig. 7c) is streakier than the first-guess patterns (Fig. 7a), and smoother with slightly weaker winds than the observed winds (Fig. 7b). As in the European case, removing the divergence from the observed winds effectively filters small-scale details. Finally, we note that the highly asymmetric 300-mb wind pattern (Fig. 7c), containing jet streaks in excess of 65 m s^{-1} to the west side of the North Dakota closed low and in the base of the Texas trough, is conducive to subsequent cyclogenesis (Newton, 1958).

In order to provide evidence that removing the divergence from the initial wind fields and deriving a consistent analysis of the mass field are useful in reducing low-frequency oscillations in the surface pressure field, we present a time series of surface pressure at a point in northwestern Missouri for forecasts (Anthes, 1978) beginning with 1) first-guess wind, geopotential and temperature (geostrophic initialization) and 2) nondivergent wind, balanced geopotential and temperature (balanced initialization) at 1200 GMT 25 January 1978. The results in Fig. 8 reveal the superiority of the balanced initial conditions over the geostrophic initial conditions, which produce unrealistic 10-mb amplitude oscillations during the first 8 h of the forecast.

Briefly alluding to the statistical summary of this case in Table 2, we note typical RMS vector wind differences between the observed and nondivergent analyses of about 5 m s^{-1}, RMS differences between first-guess and balanced heights no more than 20 m, and temperature differences on the order of 2°C except for low levels (925 and 850 mb) and the tropopause (200 mb). As we will show in the following section, the biases between the first-guess and balanced mass fields appearing in this case are not exceptional, but arise in many additional cases as well.
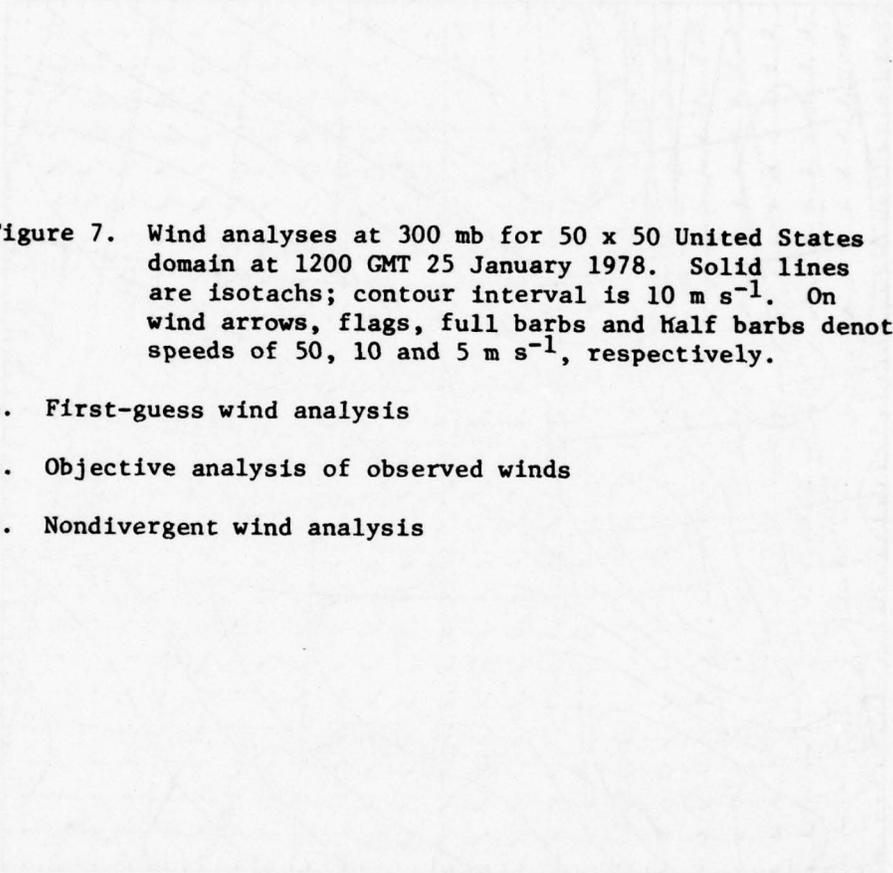
Figure 7. Wind analyses at 300 mb for 50 x 50 United States
domain at 1200 GMT 25 January 1978. Solid lines
are isotachs; contour interval is 10 m s^{-1}. On
wind arrows, flags, full barbs and half barbs denote
speeds of 50, 10 and 5 m s^{-1}, respectively.

a. First-guess wind analysis

b. Objective analysis of observed winds

c. Nondivergent wind analysis
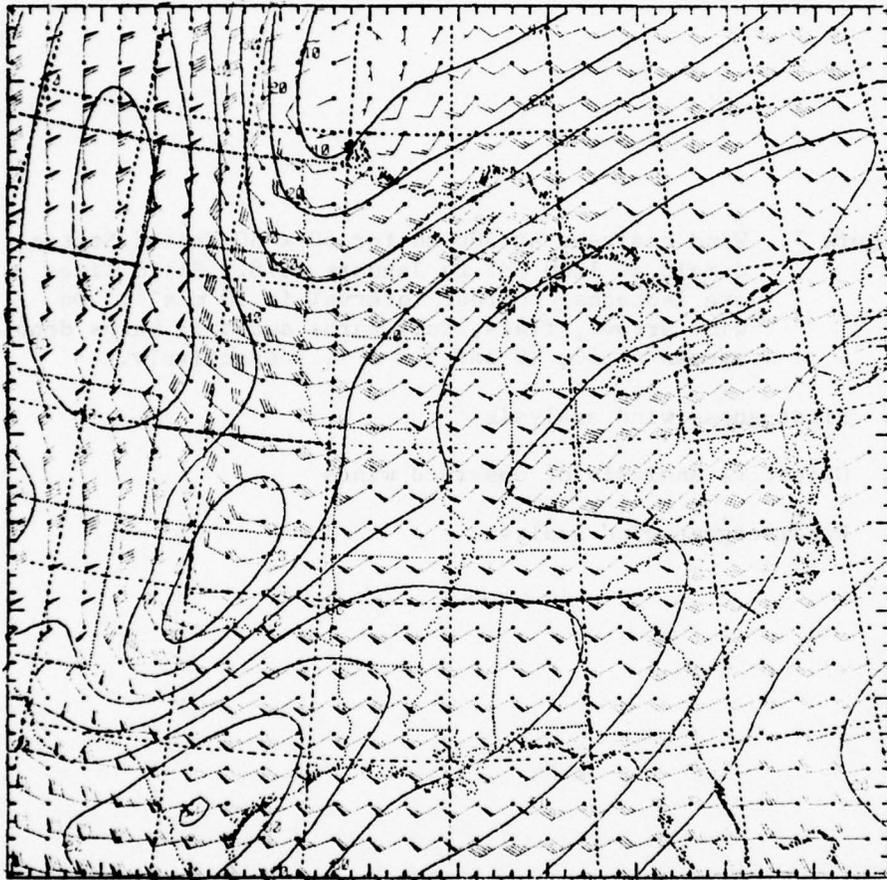
(7a)
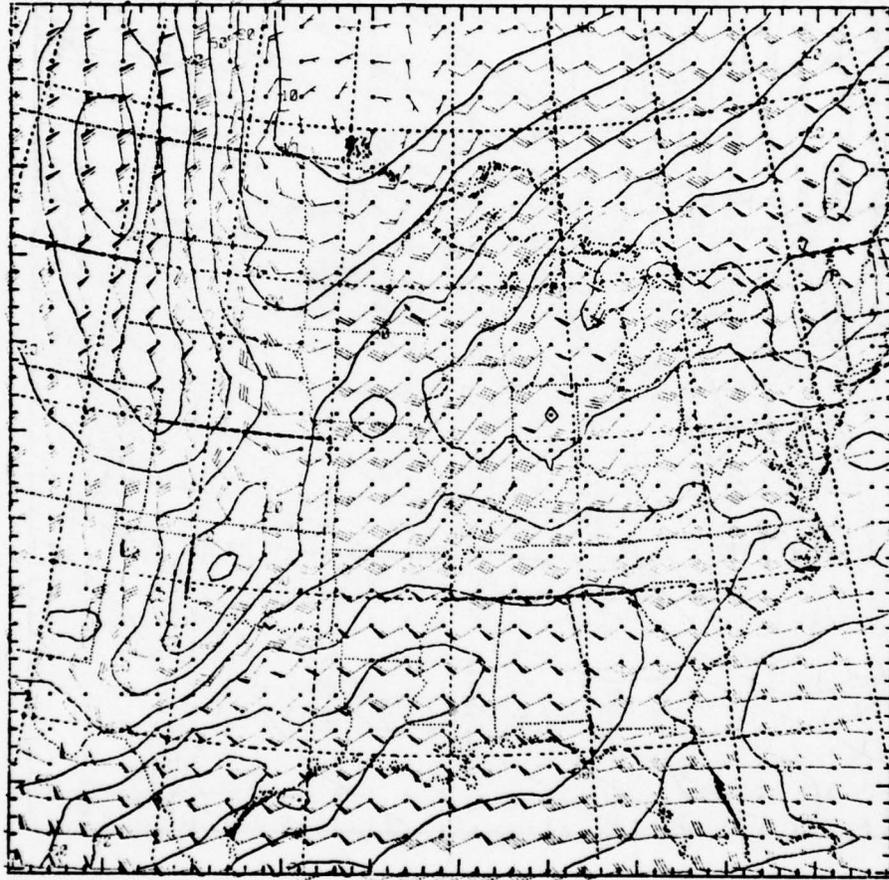
(7b)

(7c)

Figure 8. Time series of model-predicted surface pressure (mb) at a point in northwestern Missouri for geostrophic initialization (denoted by plus signs) and balanced initialization (denoted by dots) based on data for 1200 GMT 25 January 1978.

35

Table 2. Statistical summaries for first-guess, fg, and balanced, b, winds, V; heights, h; and temperatures, T; for United States domain ãt 1200 GMT 25 January 1978. Statistical quantities are defined in the Appendix.

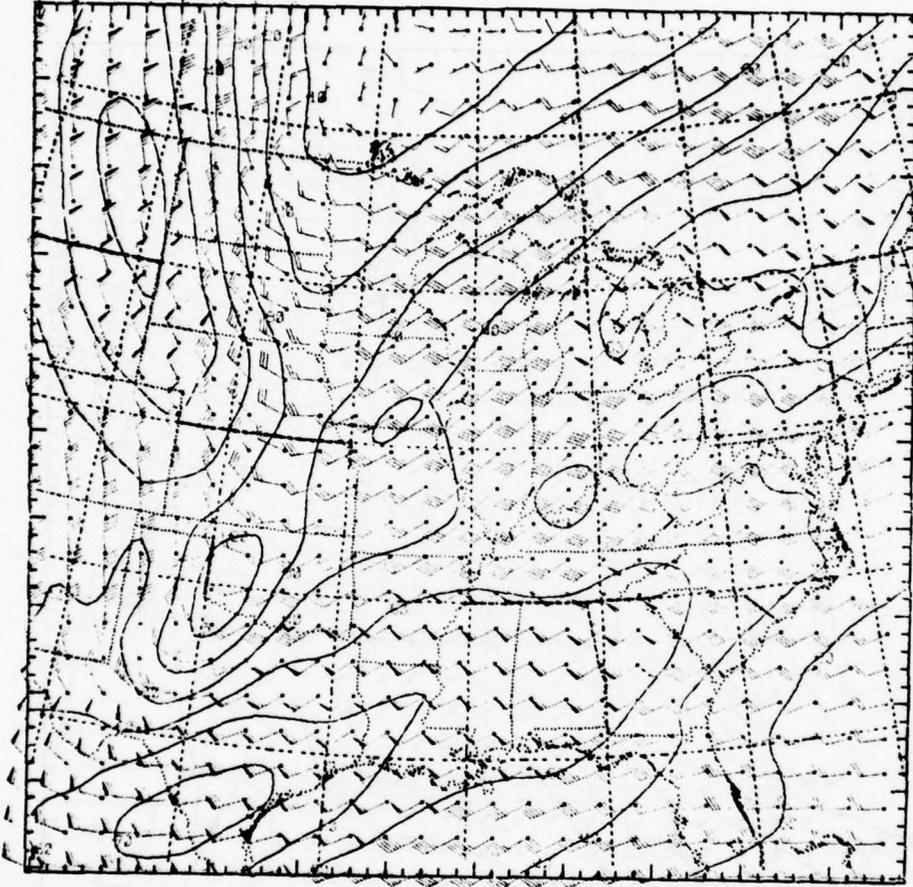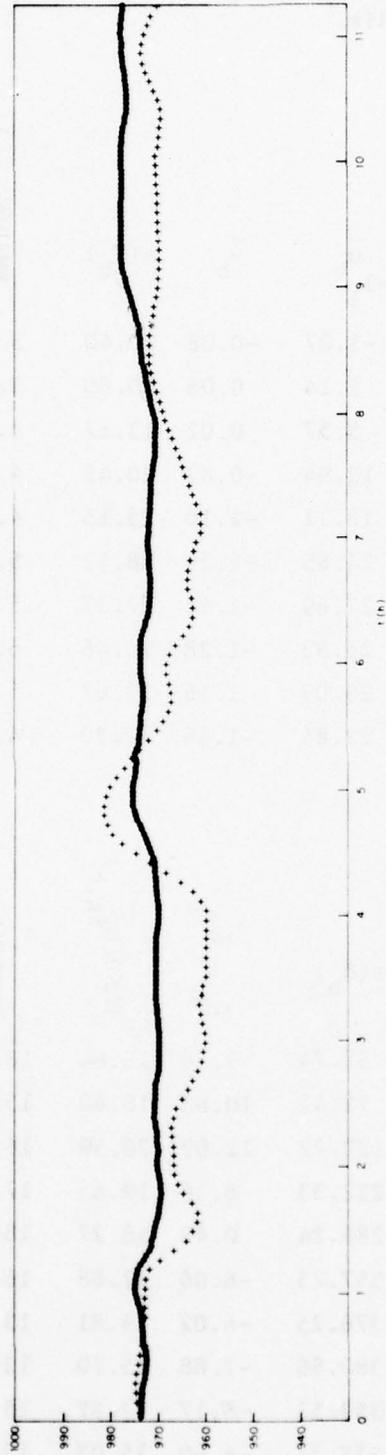| p (mb)	$\bar{u}_{fg}$	$\bar{v}_{fg}$	$s(V_{\sim fg})$ (m s^{-1})	$\bar{u}_b$	$\bar{v}_b$	$s(V_{\sim b})$	RMSD($V_{\sim fg,b}$)	RMSDC($V_{\sim fg,b}$)
925	0.62	0.87	9.97	-1.07	-0.08	10.40	3.86	3.34
850	2.86	1.03	10.38	1.14	0.06	10.80	3.98	3.46
700	7.24	1.06	12.94	5.57	0.02	13.17	3.98	3.46
500	13.83	0.54	20.33	12.94	-0.82	20.45	4.02	3.68
400	18.40	0.27	25.14	18.11	-1.10	25.15	4.15	3.91
300	24.47	-0.26	28.46	24.85	-1.39	28.12	5.02	4.88
250	27.26	-0.61	27.91	27.69	-1.41	27.37	5.63	5.55
200	29.19	-0.81	26.13	29.83	-1.28	25.46	6.05	5.99
150	28.67	-0.64	22.40	29.09	-1.16	21.67	5.71	5.67
100	23.04	-0.97	17.59	22.84	-1.48	17.20	4.63	4.60

p (mb)	$\bar{h}_{fg}$	$s(h_{fg})$	$\bar{h}_b$ (m)	$s(h_b)$	$\bar{h}_b - \bar{h}_{fg}$	RMSD($h_{fg,b}$)	RMSDC($h_{fg,b}$)	$s(h_{fg,b})$
925	745.26	61.48	754.84	57.74	9.58	16.64	13.61	0.279
850	1423.41	78.79	1434.04	72.41	10.63	18.42	15.04	0.244
700	2955.70	131.68	2967.73	122.72	12.03	20.59	16.71	0.162
500	5511.50	232.78	5519.66	222.33	8.16	19.65	17.87	0.086
400	7121.07	296.38	7121.55	288.24	0.48	18.27	18.26	0.063
300	9095.91	361.27	9089.85	357.25	-6.06	17.88	16.82	0.050
250	10301.37	378.67	10295.35	376.25	-6.02	14.81	13.53	0.039
200	11741.38	379.37	11733.50	380.86	-7.88	15.70	13.58	0.041
150	13567.14	349.19	13558.97	353.53	-8.17	17.52	15.50	0.050
100	16102.47	275.61	16095.87	277.27	-6.60	15.03	13.51	0.054

Table 2. (concluded)

p (mb)	$\bar{T}_{fg}$	$s(T_{fg})$	$\bar{T}_b$ (K)	$s(T_b)$	$\bar{T}_b - \bar{T}_{fg}$	$RMSD(T_{fg,b})$	$RMSDC(T_{fg,b})$	$s(T_{fg,b})$
925	273.30	13.89	277.37	13.05	4.07	5.21	3.26	0.387
850	271.49	12.31	272.84	12.87	1.35	2.56	2.18	0.203
700	265.97	10.72	265.65	11.20	-0.32	1.57	1.54	0.143
500	251.71	10.24	250.46	10.45	-1.25	1.70	1.16	0.164
400	241.09	9.90	239.95	9.52	-1.14	1.73	1.30	0.178
300	228.09	7.19	228.72	6.80	0.63	1,82	1.71	0.260
250	222.16	5.22	223.13	5.07	0.97	1.62	1.29	0.315
200	217.22	5.91	218.52	4.00	1.30	2.80	2.48	0.576
150	215.88	6.21	215.34	5.78	-0.54	1.31	1.20	0.219

4. Discussion of errors in determining the mass field

We tested the analysis scheme described in the previous sections in 15 European and 15 United States cases occurring between December 1977 and April 1978 (see Table 3 for times and dates) in order to reveal systematic errors. This section is devoted to analyzing temperature errors in order to evaluate the ability of the method to infer temperature patterns from the rotational part of the wind field.

Figures 9a and 9b contain first-guess and balanced temperature soundings spatially and temporally averaged over the 15 European and 15 American cases listed in Table 3. Lapse rates of temperature in both sets of soundings approximately conform to the standard atmosphere (not shown). The tropopause, located between 250 and 300 mb, is slightly lower than standard (225 mb) as expected in winter.

Both sets of mean soundings exhibit strikingly similar differences between the balanced, T_b, and first-guess, T_{fg}, temperatures. In order to magnify the time-space averaged differences, we plotted them versus ℓnp in Fig. 10. Except for the 925-mb level, the biases, $\bar{T}_b - \bar{T}_{fg}$, are nearly identical. The balanced temperatures are warmer in the upper troposphere and lower stratosphere (400-150 mb) with a maximum ~1°C at the tropopause (250 mb), and the lower troposphere (850 and 925 mb). In the middle troposphere (700-400 mb), the balanced temperatures are lower than their first-guess counterparts by as much as 0.5°C at 500 mb, which is consistent with the results cited in the two individual case studies.

Fig. 11 presents the RMS differences between T_b and T_{fg} plotted against ℓnp for the European and United States cases (compare with Tables 1 and 2). As with the bias in Fig. 10, the RMS differences are similar for the two regions except at 925 mb, where the 3.7°C difference for the American cases is particularly

Table 3. List of times and dates of European and United States cases.
The eight digit number is in the format YYMMDDHH, where YY
is the last two digits of the year; MM, month; DD, day, and
HH, hour (GMT).

Europe	United States
77121800	77121812
77121812	77121900
78011200	77121912
78011400	78012412
78011500	78012500
78011912	78012512
78012000	78012600
78012600	78012612
78021312	78012700
78021400	78021300
78030300	78021312
78030312	78021400
78040200	78021412
78040212	78030300
78040300	78030312

39

Figure 9.   Skew-T vs. ℓnp diagrams showing mean first-guess (solid
            lines) and mean balanced (dashed lines) soundings.

a.   Domain-averaged for all Mediterranean (European) cases

b.   Domain-averaged for all United States cases

40

(9a)

41

ALL U. S. CASES

(9b)

42
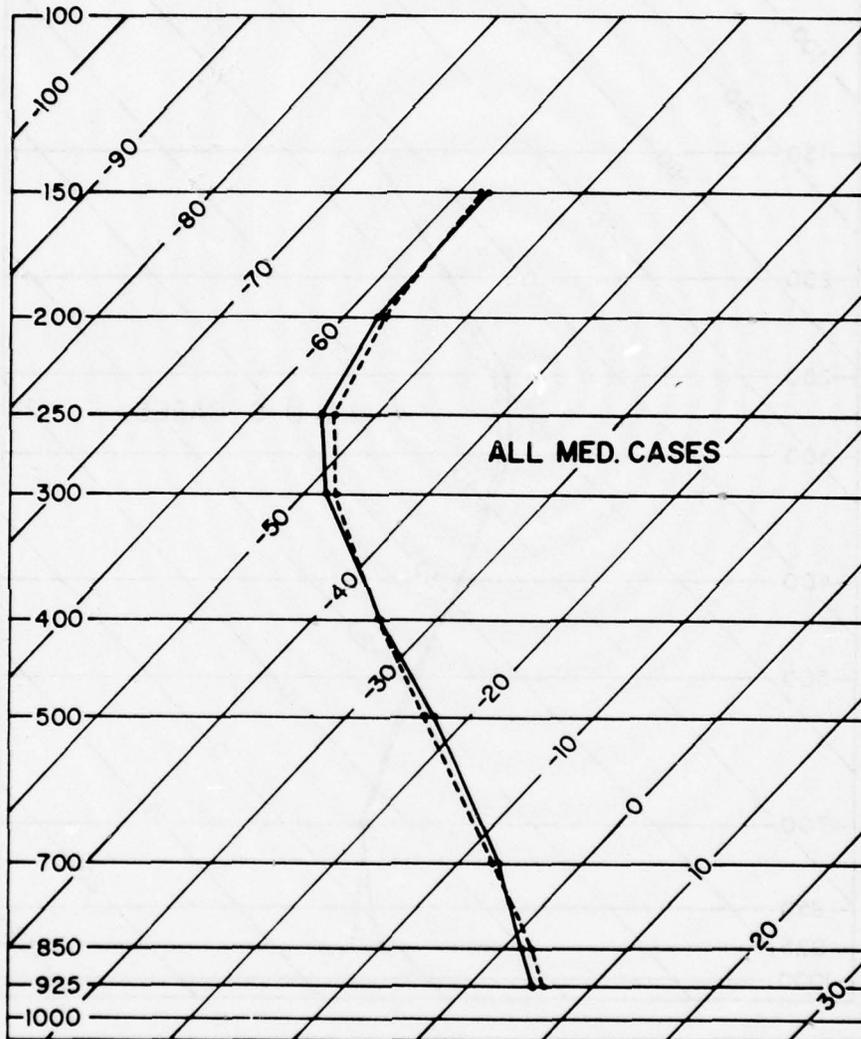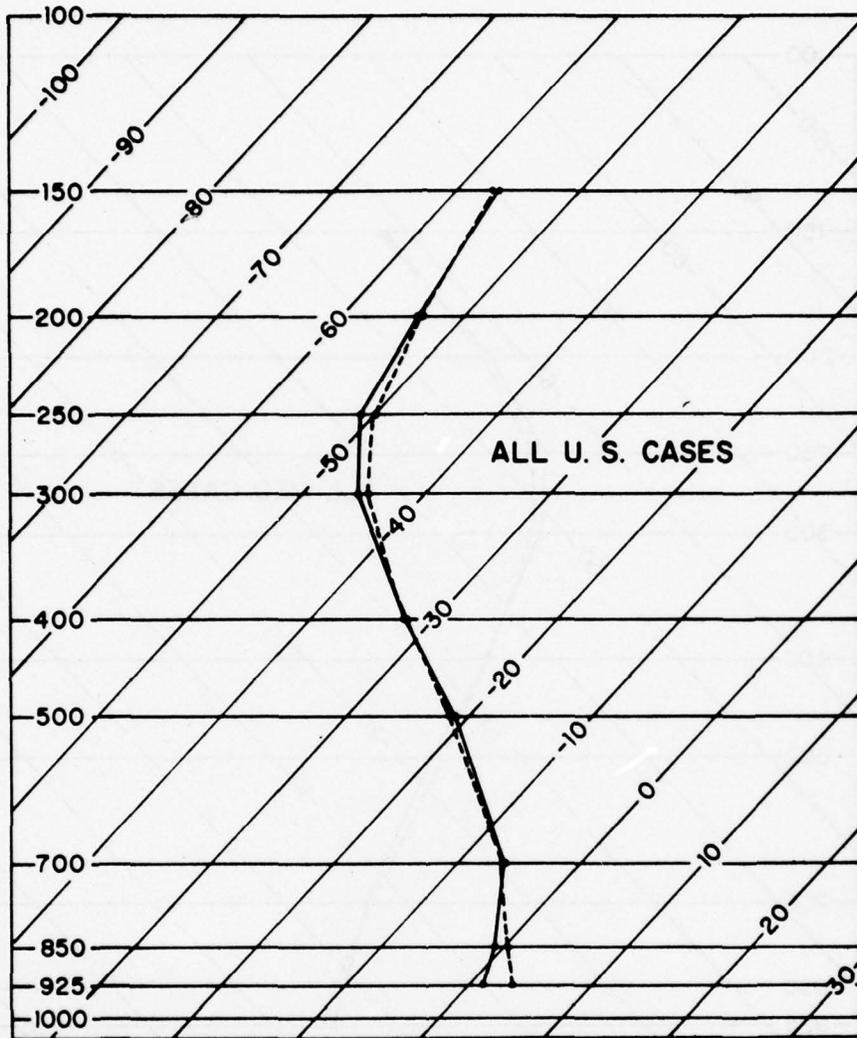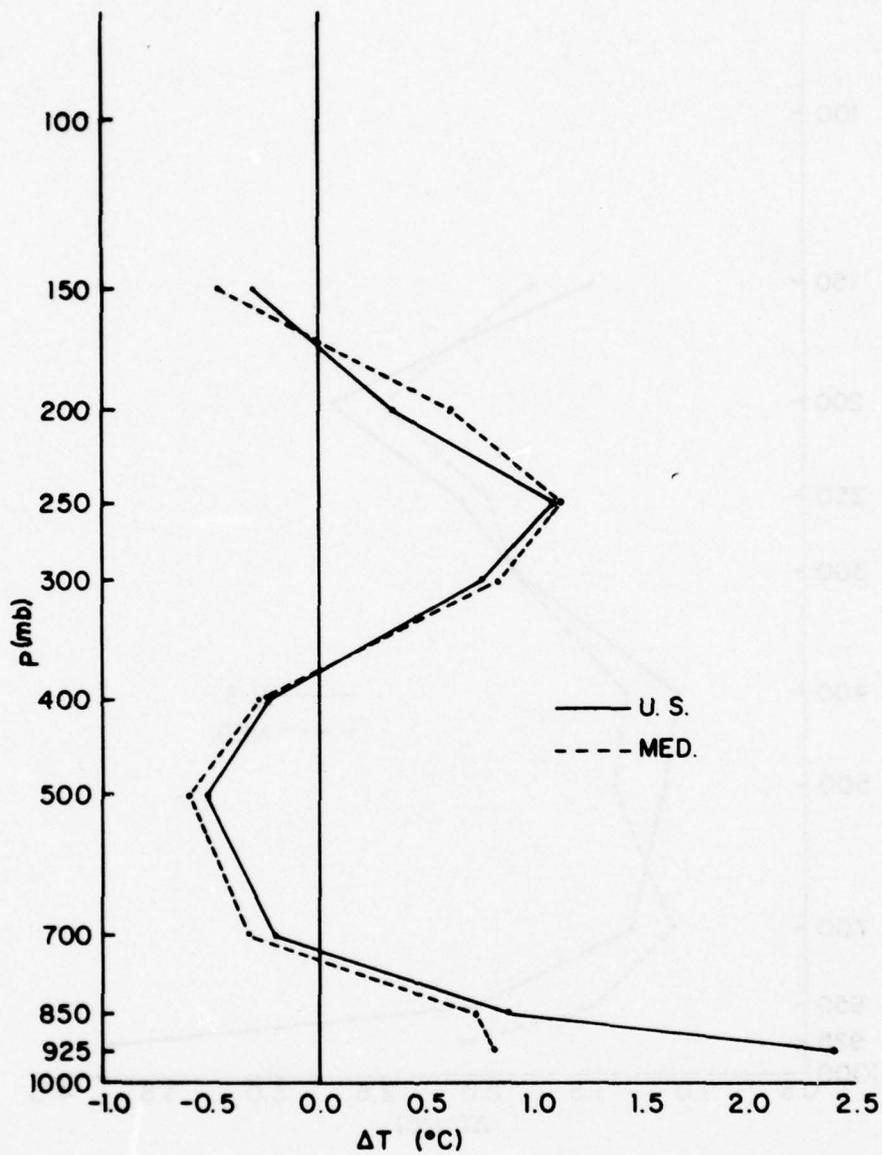
Figure 10. Differences (°C) between mean balanced and first-
guess soundings shown in Fig. 9 vs. ℓnp. Solid line
depicts United States cases; dashed line depicts
Mediterranean (European) cases.

43

Figure 11. Root-mean square differences (°C) between balanced and first-guess temperatures vs. ℓnp for all United States cases (solid line) and all Mediterranean (European) cases (dashed line).

44

disconcerting. In addition to the lowest level, errors are also large (~2.5°C) at the tropopause and least (~1.2°C) in the middle troposphere. The magnitude of these RMS differences may be compared against typical rawinsonde temperature errors of around 1°C.

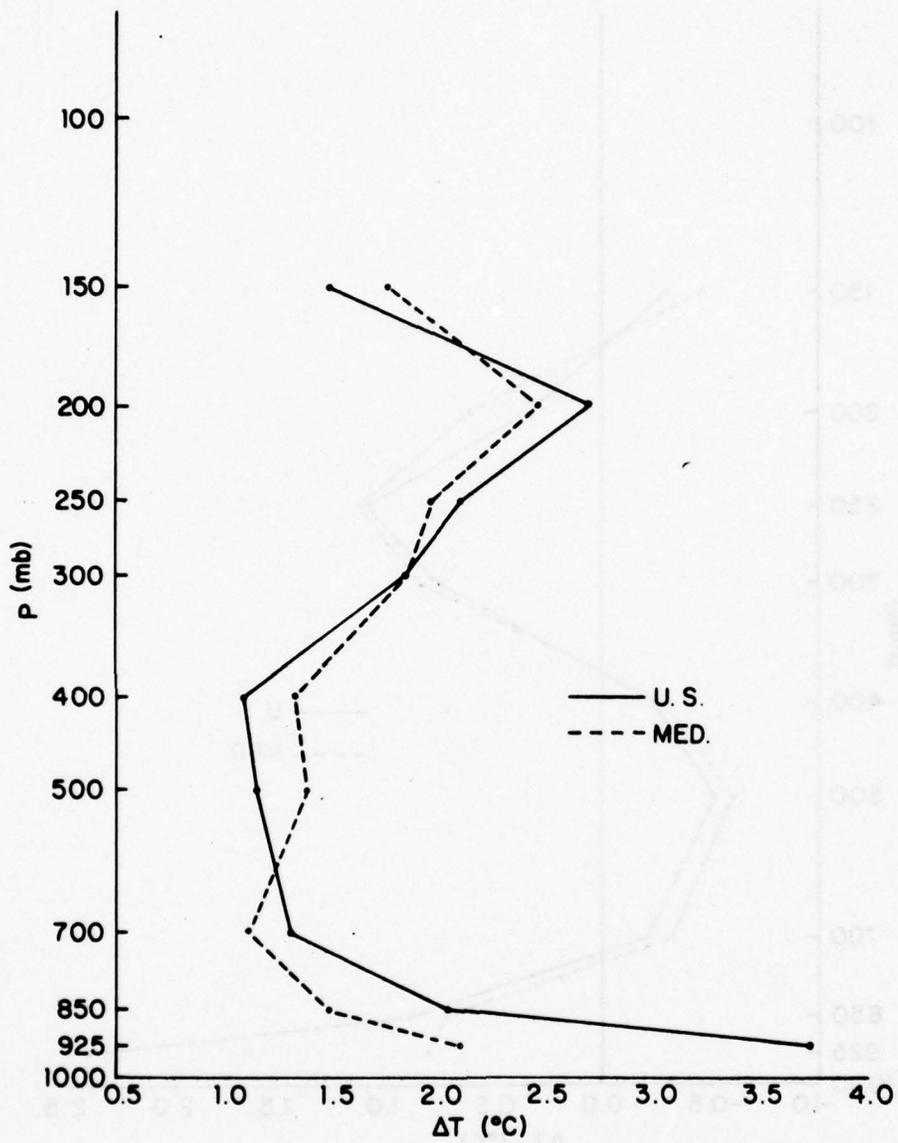The results of Figs. 10 and 11 reveal four problems requiring attention: 1) the positive bias at the tropopause; 2) the negative bias in the middle troposphere; 3) the positive bias at 925 mb; and 4) the difference between the European and American biases at 925 mb.

We begin addressing these issues by examining individual soundings for the United States case of 1200 GMT 25 January 1978. Fig. 12a and Table 4a contain the sounding for 41.9°N, 78.4°W, a location on the western Pennsylvania-New York border; Fig. 12b and Table 4b show the sounding for 47.5°N, 102.0°W in western North Dakota. In addition to exhibiting the first-guess and balanced soundings, Figs. 12a and 12b contain soundings computed from the first-guess height field. The "x's" indicate the temperature estimates at intermediate levels implied by the first-guess height field through the hydrostatic approximation, which are used to derive the temperature curve by linearly interpolating back to mandatory levels.

The tropopause in the first-guess sounding in Fig. 12a is located around 200 mb, and, consistent with the time-space averaged statistics, colder than the balanced sounding or that computed from the first-guess height field. The warm discrepancy between the balanced and first-guess tropopause temperatures may be due partly to the interpolation from the intermediate to standard pressure levels, which is unable to resolve the minimum at the tropopause. In the case of an analytically specified sounding with a constant lapse rate in the troposphere ($\gamma = 0.6\ \gamma_d$), and an isothermal lapse rate above 200 mb, differences between the hydrostatically computed and specified soundings were less than 0.1°C

45

Figure 12. Skew-T vs. ℓnp diagrams for two locations at 1200 GMT
25 January 1978. Solid line depicts sounding computed
from first-guess heights; "x's" denote layer-averaged,
hydrostatically derived temperatures used to construct
this sounding. Long dashes denote first-guess sounding;
short dashes denote balanced sounding.

a. Sounding at 41.9°N, 78.4°W

b. Sounding at 47.5°N, 102.0°W

(12a)

(12b)

48
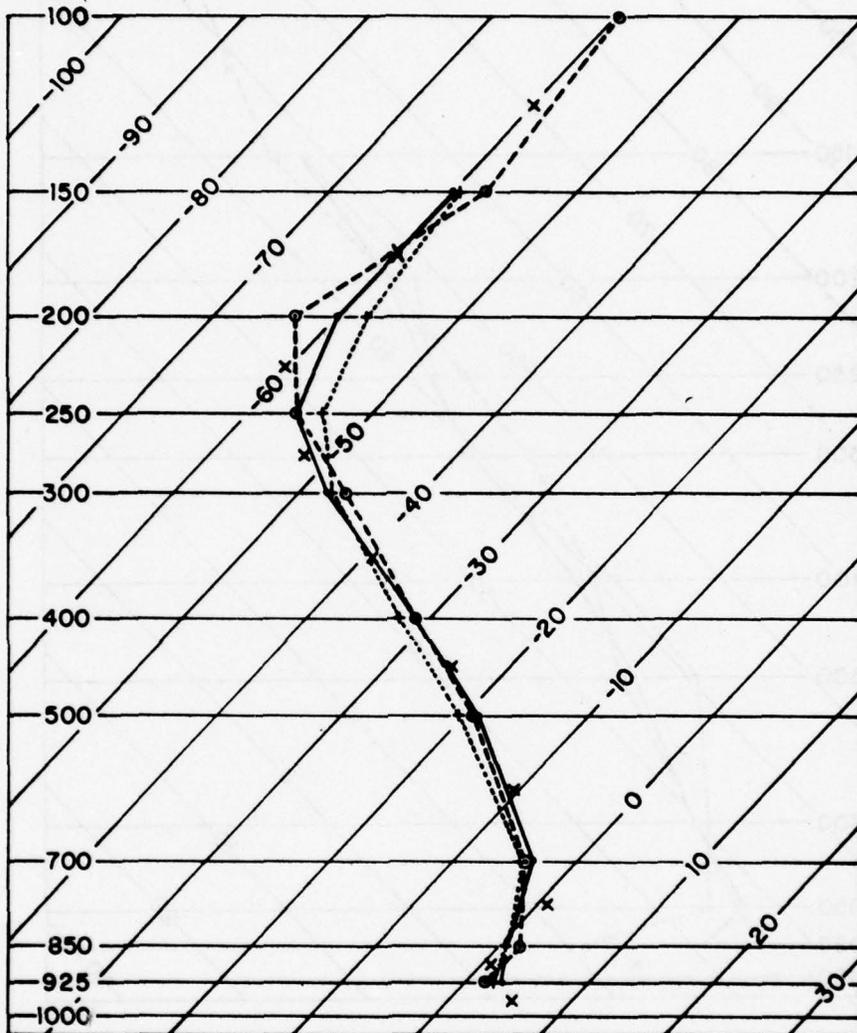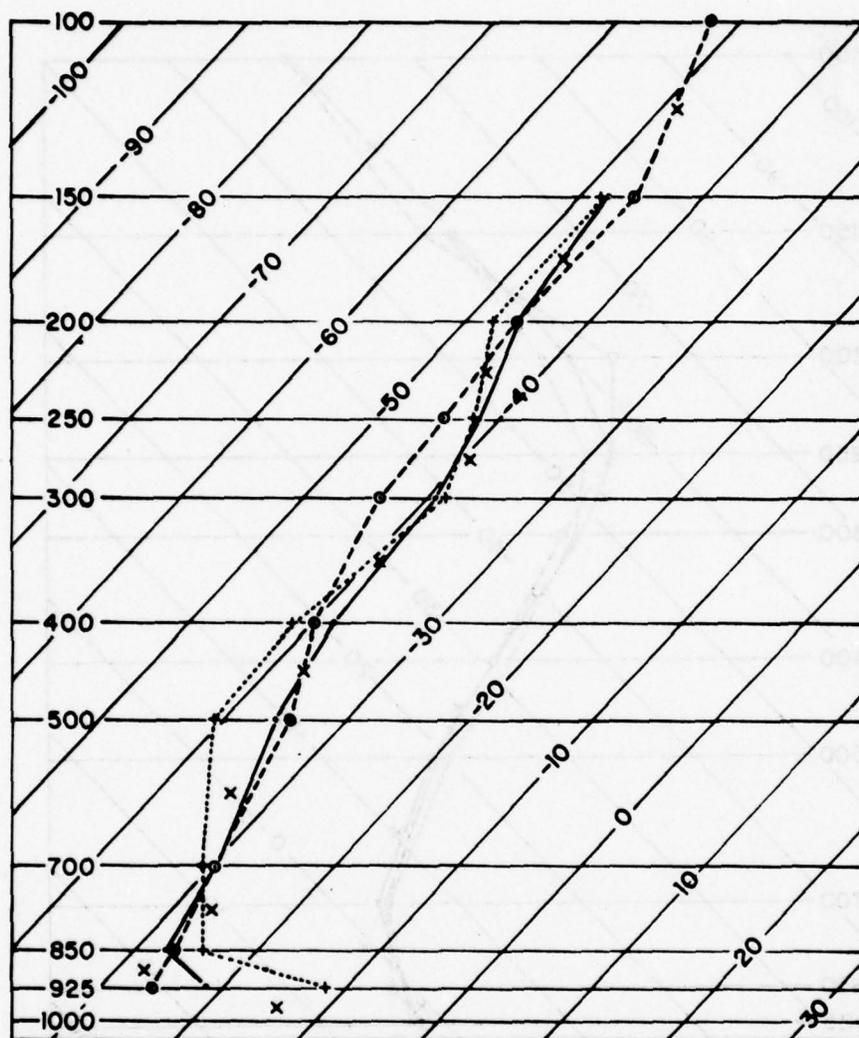
Table 4. Sounding data for first-guess, fg, and balanced, b, tempera-
tures, T, and heights, h, for 1200 GMT 25 January 1978.
a. Sounding at 41.9°N, 78.4°W.
b. Sounding at 47.5°N, 102.0°W.

	p (mb)	T_{fg}	T_b (°C)	$T_b - T_{fg}$	h_{fg}	h_b (m)	$h_b - h_{fg}$
a.	925	1.7	2.1	0.4	706	702	-4
	850	1.8	0.6	-1.2	1384	1380	-4
	700	-4.1	-4.2	-0.1	2942	2934	-8
	500	-19.5	-20.6	-1.1	5530	5513	-17
	400	-31.1	-32.7	-1.6	7153	7126	-27
	300	-46.2	-47.3	-1.1	9123	9086	-37
	250	-56.1	-54.0	2.1	10303	10270	-33
	200	-63.4	-57.7	5.7	11694	11682	-12
	150	-57.1	-59.5	-2.3	13493	13492	-1
	100	-59.7			16025		
b.	925	-25.9	-11.7	14.2	742	788	46
	850	-26.9	-24.3	2.6	1350	1407	57
	700	-29.8	-30.7	-0.9	2751	2810	59
	500	-34.6	-40.7	-6.1	5109	5129	20
	400	-39.9	-41.6	-1.7	6651	6637	-14
	300	-43.9	-38.5	5.4	8623	8597	-26
	250	-44.6	-42.0	2.6	9872	9856	-16
	200	-45.8	-47.7	-1.9	11366	11331	-35
	150	-45.4	-48.0	-2.6	13273	13228	-45
	100	-52.3			15936		

49

in the troposphere (at and below 250 mb) and 2.3°C at 200 mb, the assumed tropo-pause level. In the real atmosphere we may expect this difference to be smaller since the change in lapse rate at the tropopause is usually less abrupt. A related source of error at the tropopause is revealed in Fig. 12b, where the balanced and hydrostatically computed temperatures are quite similar but warmer than the first-guess temperature at 300 and 250 mb. This latter problem suggests an inconsistency between our method of hydrostatically computing temperatures and FNWC's method of relating heights and temperatures. Whether or not this latter problem is systematic is unknown.

The former sources of error are a result of vertical truncation and would occur even if the balanced heights were perfect. A final line of speculation concerning the positive bias in the high troposphere can be attributed to errors in the balanced heights. Ignoring vertical truncation errors, we can relate the discrepancy in the temperature to the discrepancy in the thickness hydro-statically so that

$$ \frac{\partial h'}{\partial \ell np} = - \frac{RT'}{g} , \tag{13} $$

where the prime denotes the difference between a balanced and first-guess quan-tity $[(\;)' = (\;)_b - (\;)_{fg}]$. According to (13), temperature differences T' are positive (negative) above (below) minima in h'. For the sounding in Fig. 12a, h' has a minimum of -37 m at 300 mb increasing to -1 m at 150 mb (Table 4a), which, from (13), implies $T' = 1.8°C$. On the other hand, h' in-creases in the lower troposphere to -4 m at 850 mb from the 300 mb value, implying $T' = -1.1°C$ between these two levels. The trend is similar in Fig. 12b and Table 4b where balanced heights are higher in the lower troposphere and lower in the high troposphere than the first-guess values ($h' = 59$ m at 700 mb, -26 m at 300 mb implying $T' = -3.4°C$), a situation that can explain the negative

50

bias in the middle troposphere and the positive bias at the surface and tropo-
pause. This trend is evident in the domain-averaged height differences for
this time as well (see Table 2).

The temperature calculation at 925 mb is extremely sensitive to height
errors since the temperature is computed over a thin layer. For example, for
$h' = 10$ m and the sea-level pressure equal to 1013 mb, $T' = 3.8°C$ (see Table 2
for comparison with 925 mb height and temperature statistics). Moreover, these
temperature errors become more serious in the vicinity of low pressure systems.
If the sea-level pressure were 1000 mb, $h' = 10$ m, then T' would equal 4.4°C.

The order of magnitude and sign of the 46-m height discrepancy at 925 mb
for the North Dakota sounding (Table 4b) can be explained by the divergence and
friction terms neglected in forming the balance equation (12). If the
tilting terms are unimportant, the bias in geopotential ϕ' is approximately
given by

$$\nabla^2\phi' = D^2 + \frac{dD}{dt} + kD , \qquad (14)$$

where D is the horizontal divergence and k a linear friction coefficient
given by $C_D|V|/H$, where C_D is a drag coefficient, $|V|$ surface wind speed
and H boundary layer depth. A crude scale analysis allows us to revise (14)
into

$$\overset{\text{(1)} \quad \text{(2)} \quad \text{(3)}}{\frac{16\phi'}{L^2} \approx -D^2 - \frac{4VD}{L} - kD} . \qquad (15)$$

Here L is the wavelength of a surface cyclone, and V a phase propagation
speed so that the time scale, $T = \frac{L}{4V}$, for the parcel derivative is assumed
to be due to the local variation at a point. For $L \sim 2000$ km (Fig. 5),
$V \sim 10$ m s^{-1}, $k \sim 1\times10^{-4}$ s^{-1} ($C_D = 5\times10^{-3}$, $H = 500$ m),and $D \sim -1\times10^{-5}$ s^{-1}

(divergence appropriate for medium-intensity synoptic systems [Petterssen, 1956]),
T is about 14 h and

$$\begin{array}{ccc} (1) & (2) & (3) \end{array}$$

$$h' \sim -2.5 \text{ m} + 5 \text{ m} + 25 \text{ m} = 27.5 \text{ m} . \qquad (16)$$

From the above result, we see that ignoring frictional effects in the planetary
boundary layer (PBL) dominates as a source of error. We can use the results of
the scale analysis to explain the differences in the 925-mb temperature biases
between the European and American cases. Although we do not offer quantitative
evidence, inspection of the individual cases reveals that the American cases
are dominated by deeper, more intense low pressure systems, where ignoring sur-
face friction in the presence of low sea-level pressure magnifies the positive
bias between the balanced and first-guess 925-mb temperatures. Furthermore,
we note that the 925-mb temperature bias is negligible for the United States
sounding (Fig. 12a, Table 4a) over a flat sea-level pressure field (Fig. 5) com-
pared to the sounding (Fig. 12b, Table 4b) where the cyclonic curvature is strong.

A similar calculation may be performed for the tropopause level (~300 mb).
Taking $L \sim 4000$ km (Fig. 6a), $V \sim 40$ m s^{-1} (here V is a wind velocity so that
T is an advective time scale), $k = 0$, and $D \sim 1 \times 10^{-5}$ s^{-1}, T is about 7 h and

$$\begin{array}{ccc} (1) & (2) & (3) \end{array}$$

$$h' \sim -10 \text{ m} + - 40 \text{ m} + 0 \text{ m} = - 50 \text{ m} . \qquad (17)$$

The major omission in this case is the time derivative of the divergence follow-
ing parcel trajectories.

In summary, the discrepancies between the balanced and first-guess temperature analyses can be attributed[1] to 1) vertical truncation or interpolation error in attempting to resolve the discontinuity in lapse rate at the tropopause, 2) ignoring the divergent part of the wind and surface friction in determining geopotential, and 3) inconsistencies between our method and FNWC's method for hydrostatically relating heights and temperatures.

5. Summary and suggestions for future investigation

Extensive tests of solving for the mass field from the rotational part of the wind field over a large number (30) of cases indicate that RMS heights and temperatures can be resolved within 20 m and 2°C, respectively. Errors in boundary layer temperature may be larger locally on account of neglecting friction and because of the shallow depth of the layer. The above figures apply to rectangular mid-latitude domains on the order of 4000 km on a side with 60-km grid resolution. The boundary geopotential are assumed known from a reliable large-scale analysis.

There is strong evidence that including an analysis of the divergent part of the wind and surface friction would result in an improvement in determining the temperature field. A possibility for including the divergent part of the wind in the analysis in a manner consistent with filtering gravity waves lies in experimenting with the vorticity form of the balance equation,

$$\nabla^2 \phi = \zeta(\zeta+f) + \hat{k} \cdot \nabla(\zeta+f) \times \underset{\sim}{V} - \nabla^2 (\frac{\underset{\sim}{V} \cdot \underset{\sim}{V}}{2}) + \nabla \cdot \underset{\sim}{F}_r \quad , \tag{18}$$

where $\underset{\sim}{F}_r$ is a friction term and we have assumed that $\frac{\partial D}{\partial t} = 0$. Saha and Suryanarayana (1971) compared (18) with $\underset{\sim}{F}_r = 0$ with the nonlinear balance

---

[1]This list excludes the effect of errors in the rotational part of the wind on the derived geopotential. We have assumed these errors are random and do not contribute to the bias in the derived temperatures.

53

equation (12), the linear balance equation and quasi-geostrophic form of the balance equation, when solving for geopotential in the tropics. They found (18) to give results slightly superior to the nonlinear and linear forms, while the quasi-geostrophic version yielded results inferior to the three former balance equations.

Despite the improvement in the temperature patterns expected from including the divergent part of the wind and surface friction in the analysis, determining the former is a vexing problem because it is masked by the errors in the wind data. The method devised by Endlich (1967), which adjusts a vector field to imposed values of vorticity or divergence may offer a viable alternative. Adjustment of the horizontal wind components to satisfy boundary conditions on the vertical velocity (O'Brien, 1970; Fankhauser, 1974) is an additional possibility.

Finally, we point out that the gain in accuracy with our approach of solving for mass from winds results from integrating the velocity to obtain stream function and geopotential, a process that tends to smooth small-scale observational errors. We take a loss in accuracy, however, when we vertically differentiate the geopotential to obtain temperature, because differentiating real data tends to introduce noise. Despite such inherent limitations, our method for inferring the mass field is competitive with existing analysis schemes, and has the potential for further improvement.

54

APPENDIX

1. Comments on solutions to Poisson equations

When solving for the nondivergent wind and the balanced geopotential, we must solve a Poisson equation

$$\nabla^2 \phi(x,y) = F(x,y) \tag{19}$$

given ϕ on the lateral boundaries. We proceed to interpret the analytic solution to (19) in order to help understand the numerical results obtained through the analysis procedure.

For a rectangular domain with $0 \le x \le L$ and $0 \le y \le D$, the solution to (1) is

$$
\phi(x,y) = \frac{2}{D} \sum_{n=1}^{\infty} \frac{\sinh \frac{n\pi}{D}(L-x)}{\sinh \frac{n\pi L}{D}} \sin \frac{n\pi y}{D} \left(\int_0^D \phi(0,y') \sin \frac{n\pi y'}{D} \, dy' \right)
$$

$$
+ \frac{2}{D} \sum_{n=1}^{\infty} \frac{\sinh \frac{n\pi}{D} x}{\sinh \frac{n\pi L}{D}} \sin \frac{n\pi y}{D} \left(\int_0^D \phi(L,y') \sin \frac{n\pi y'}{D} \, dy' \right)
$$

$$
+ \frac{2}{L} \sum_{n=1}^{\infty} \frac{\sinh \frac{n\pi}{L}(D-y)}{\sinh \frac{n\pi D}{L}} \sin \frac{n\pi x}{L} \left(\int_0^L \phi(x',0) \sin \frac{n\pi x'}{L} \, dx' \right)
$$

$$
+ \frac{2}{L} \sum_{n=1}^{\infty} \frac{\sinh \frac{n\pi y}{L}}{\sinh \frac{n\pi D}{L}} \sin \frac{n\pi x}{L} \left(\int_0^L \phi(x',D) \sin \frac{n\pi x'}{L} \, dx' \right)
$$

$$
- \frac{4LD}{\pi^2} \sum_{n=1}^{\infty} \sum_{m=1}^{\infty} \frac{\sin \frac{n\pi x}{L} \sin \frac{m\pi y}{D}}{L^2 m^2 + D^2 n^2} \left(\int_0^D \int_0^L F(x',y') \sin \frac{n\pi x'}{L} \sin \frac{m\pi y'}{D} \, dx' dy' \right) .
$$

$$\tag{20}$$

56

The first four terms on the right are the contributions of each lateral boundary condition to the solution. The final term is the component of the solution due to the forcing in the interior.

Because (19) is linear, we may interpret (20) for a single harmonic without loss of generality. We see that the influence of the right lateral boundary condition, $\phi(L,y)$ [the second term on the right of (20)] damps exponentially with distance from the boundary at a rate determined by the wavenumber of the harmonic representing $\phi(L,y)$. This point is illustrated in Fig. 13, where the term controlling the damping of the boundary condition $\phi(L,y)$ is graphed as a function of wavenumber $\frac{n\pi L}{D}$ and normalized distance $\frac{x}{L}$. For a given distance from the boundary, for increasing wavenumber, the value of the function decreases.

The implications of the preceding arguments are:

1) The influence of the boundary conditions on the solution decreases exponentially with distance from the boundaries.

2) It is important to specify the large-scale (low wavenumber) variation of the boundary conditions accurately, since amplitude errors for low wavenumber components of the boundary conditions damp less rapidly.

The preceding analysis is modified slightly when a discrete domain is considered (R. T. Williams, personal communication). The Laplace equation that is solved in the continuous case to isolate the influence of the boundary conditions becomes

$$\phi_{j+1k} + \phi_{jk+1} + \phi_{jk-1} + \phi_{j-1k} - 4\phi_{jk} = 0 . \tag{21}$$

In (21), which applies to a grid with uniform spacing such that $x = j\Delta s$ and $y = k\Delta s$, one can show that

$$\phi_{jk} = A\, e^{\mu j\Delta s}\, e^{i\lambda k\Delta s} \tag{22}$$

57
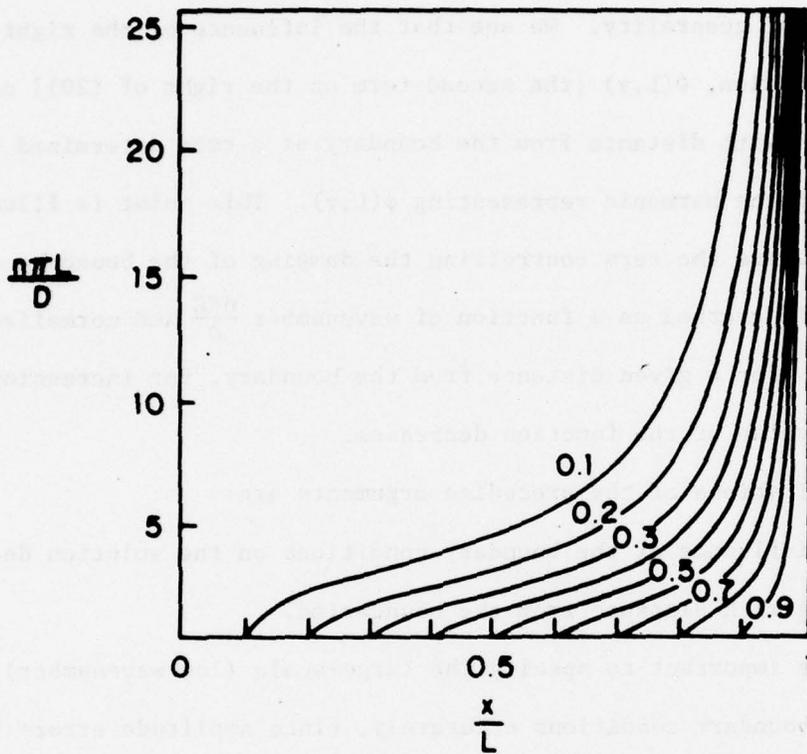
Figure 13. Plot of contours of $f(\frac{n\pi L}{D}, \frac{x}{L}) = \dfrac{\sinh \frac{n\pi L}{D} \frac{x}{L}}{\sinh \frac{n\pi L}{D}}$ repre-
senting the frictional damping of
the boundary condition at x/L = 1 as a function of
distance normal to the boundary and wavenumber. See
text for definition of symbols.

is a solution to (21) provided that

$$\cosh \mu\Delta s = 2 - \cos \lambda\Delta s \ . \tag{23}$$

In (22), A is a complex constant, $\lambda = \dfrac{2\pi}{L_y}$, where L_y is wavelength in the y direction such that $L_y = K\Delta s$, and $\mu = \dfrac{2\pi}{L_x}$ with L_x wavelength in the x direction.

We can write

$$L_x = rL_y \tag{24}$$

or

$$\mu = \frac{\lambda}{r} \tag{25}$$

Fig. 14 is a graph of r versus K as determined by (23). For short wavelengths with respect to the grid the damping is slower than in the continuous case with the largest difference for $2\Delta s$ waves ($r \stackrel{\sim}{=} 1.8$). For waves longer than $10\Delta s$ the differences between the continuous and discrete cases are negligible. The conclusions drawn from the continuous case apply to the discrete case provided that the correction for short waves shown in Fig. 14 is considered.

2. Definitions of statistical quantities

For a quantity α we denote the mean over the domain as $\bar{\alpha}$. The mean-square difference (MSD) between two sets of α data is

$$MSD(\alpha_{1,2}) = \overline{|\alpha_1 - \alpha_2|^2} \ , \tag{26}$$

where 1 and 2 identify their respective data sets. The MSD corrected for the mean is denoted as

$$MSDC(\alpha_{1,2}) = \overline{|(\alpha_1 - \bar{\alpha}_1) - (\alpha_2 - \bar{\alpha}_2)|^2} \tag{27}$$

59
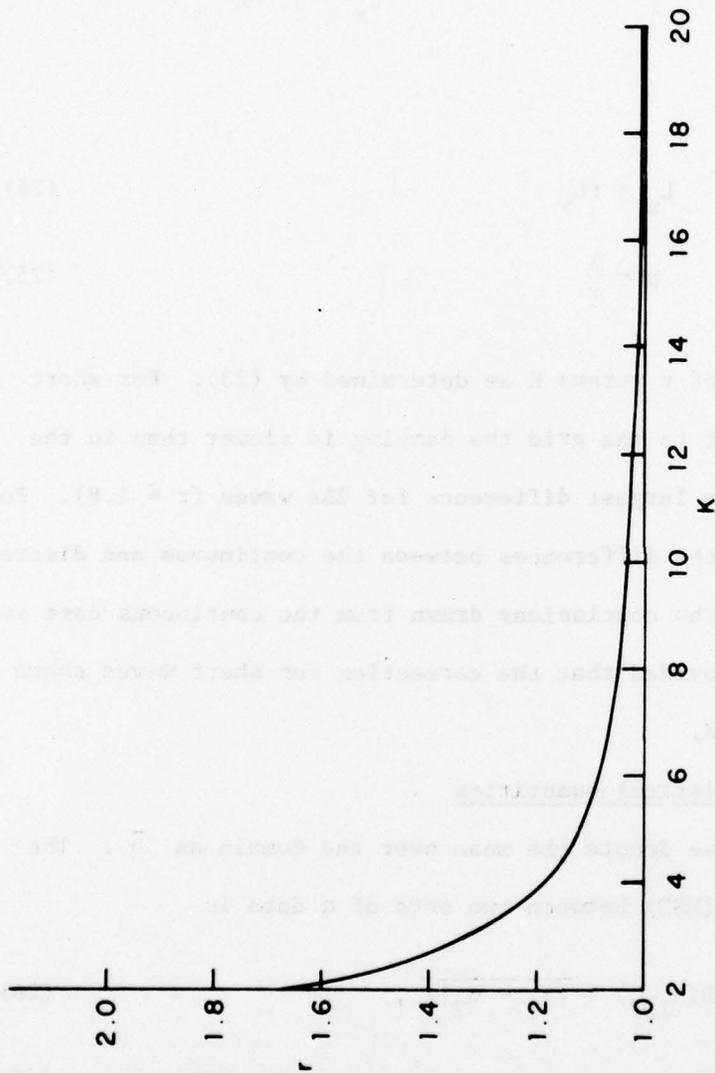
Figure 14. Plot of r, representing the ratio of the damping rate of a boundary harmonic with distance in the continuous case to that in the discrete case as given by (23), vs. K, where K is wavelength of a boundary harmonic in grid units.

and the variance of α is written as

$$s^2 = \overline{|\alpha - \bar{\alpha}|^2} \,. \tag{28}$$

The above definitions apply to scalar or vector quantities provided that one invokes the appropriate definition of the absolute value operator.

If one defines a dimensionless skill score

$$s^2 = \frac{MSD(\alpha_{1,2})}{s_1 \, s_2} \,, \tag{29}$$

it can be shown that

$$s^2 = \frac{s_1}{s_2} + \frac{s_2}{s_1} - 2r + \frac{|\bar{\alpha}_1 - \bar{\alpha}_2|^2}{s_1 \, s_2} \,, \tag{30}$$

where r is the correlation between α_1 and α_2 , so that

$$r = \frac{\overline{(\alpha_1 - \bar{\alpha}_1) \cdot (\alpha_2 - \bar{\alpha}_2)}}{s_1 \, s_2} \,. \tag{31}$$

Defining a skill score corrected for the mean as

$$s_c^{\,2} = \frac{MSDC\,(\alpha_{1,2})}{s_1 \, s_2} \,, \tag{32}$$

one may show that

$$s_c^{\,2} = \frac{s_1}{s_2} + \frac{s_2}{s_1} - 2r \tag{33}$$

so that

$$s^2 = s_c^{\,2} + \frac{|\bar{\alpha}_1 - \bar{\alpha}_2|^2}{s_1 \, s_2} \,. \tag{34}$$

In order to interpret the skill score S, defined in (29), we let the subscripts 1 and 2 denote the predicted (or derived) field and the verification field, respectively. For a given MSD, dividing by the product of the standard deviations of both fields attributes greater skill (smaller value of S) when the variation of the fields about their mean is larger, and reproducing the verification field is inherently more difficult. According to (30), S is equal to zero (a perfect score) when the standard deviations of the derived and verification fields are equal, their means are equal, and the correlation between them is equal to one. Moreover, we observe that the sum of the first two terms in (30) is a minimum (equal to 2) when $s_1 = s_2$. Therefore, (29) does not reward a conservative estimate of the verification field ($s_1 < s_2$), while the MSD itself tends to be smaller for a smoother predicted pattern.

REFERENCES

Anthes, R. A., 1976: Initialization of mesoscale models with real data. <u>Preprints Sixth Conf. Weather Forecasting and Analysis</u>, Amer. Meteor. Soc., 156-160.

Anthes, R. A., 1978: Tests of a mesoscale model over Europe and the United States, Naval Postgraduate School Technical Report NPS63-78004.

Anthes, R. A., and T. T. Warner, 1978: The development of hydrodynamic models suitable for air pollution and other mesometeorological studies. <u>Mon. Wea. Rev.</u>, <u>106</u>, (in press).

Bedient, H.A., and J. Vederman, 1964: Computer analysis and forecasting in the tropics. <u>Mon. Wea. Rev.</u>, <u>92</u>, 565-577.

Brown, J. A., and J. R. Neilon, 1961: Case studies of numerical wind analysis. <u>Mon. Wea. Rev.</u>, <u>89</u>, 83-90.

Cline, A. K., 1974: Scalar- and planar-valued curve fitting using splines under tension. <u>Commun. ACM</u>, <u>17</u>, 218-220.

Elsberry, R. L., and G. W. Ley, 1976: On the strategy of initializing nested grid meshes in numerical weather prediction. <u>Mon. Wea. Rev.</u>, <u>104</u>, 797-799.

Endlich, R. M., 1967: An iterative method for altering the kinematic properties of wind fields. <u>J. Appl. Meteor.</u>, <u>6</u>, 837-844.

Fankhauser, J. C., 1974: The derivation of consistent fields of wind and geopotential height from mesoscale rawinsonde data. <u>J. Appl. Meteor.</u>, <u>13</u>, 637-646.

Haltiner, G. J., 1971: <u>Numerical Weather Prediction</u>, Wiley, 317 pp.

Kesel, P. G., and F. J. Winninghoff, 1972: The Fleet Numerical Weather Central operational primitive-equation model. <u>Mon. Wea. Rev.</u>, <u>100</u>, 360-373.

Newton, C. W., 1958: Variations in frontal structure of upper level troughs. <u>Geophysica</u>, <u>6</u>, 357-375.

O'Brien, J. J., 1970: Alternative solutions to the classical vertical velocity problem. <u>J. Appl. Meteor.</u>, <u>9</u>, 197-203.

Petterssen, S., 1956: <u>Weather Analysis and Forecasting</u>, Vol. 1, Mc-Graw-Hill, 266 pp.

Phillips, N. A., 1958: Geostrophic errors in predicting the Appalachian storm of Nov. 1950. <u>Geophysics</u>, <u>5</u>, 389-405.

Rosmond, T. E., and F. D. Faulkner, 1976: Direct solution of elliptic equations by block cyclic reduction and factorization. Mon. Wea. Rev., 104, 641-649.

Saha, K., and R. Suryanarayana, 1971: Numerical solutions of geopotential with different forms of balance relationships in the tropics. J. Meteor. Soc. Japan, 49, 510-515.

Shuman, F. G., 1957: Numerical methods in weather prediction: I. The balance equation. Mon. Wea. Rev., 85, 329-332.

Wagner, A. J., 1978: Weather and circulation of January 1978. Mon. Wea. Rev., 106, 579-585.

12. Atmospheric Sciences Library   1
     National Oceanic and Atmospheric Administration
     Silver Spring, Maryland 20910

13. Dr. F. P. Bretherton   1
     National Center for Atmospheric Research
     P. O. Box 3000
     Boulder, Colorado 80303

14. Dr. John Brown   1
     National Meteorological Center/NOAA
     World Weather Building
     Washington, D. C. 20233

15. Dr. C.-P. Chang, Code 63Cj   1
     Department of Meteorology
     Naval Postgraduate School
     Monterey, California 93940

16. Dr. Fred Shuman, Director   1
     National Meteorological Center
     World Weather Building
     Washington, D. C. 20233

17. Dr. R. L. Elsberry, Code 63Es   2
     Department of Meteorology
     Naval Postgraduate School
     Monterey, California 93940

18. Dr. D. Williamson   1
     National Center for Atmospheric Research
     P. O. Box 3000
     Boulder, Colorado 80303

19. Mr. D. Baumhefner   1
     National Center for Atmospheric Research
     P. O. Box 3000
     Boulder, Colorado 80303

20. Dr. W. L. Gates   1
     Department of Meteorology
     Oregon State University
     Corvallis, Oregon 97331

21. Dr. R. Somerville   1
     National Center for Atmospheric Research
     P. O. Box 3000
     Boulder, Colorado 80303

22. Dr. G. J. Haltiner, Code 63Ha   5
     Chairman, Department of Meteorology
     Naval Postgraduate School
     Monterey, California 93940

23. Dr. R. L. Haney, Code 63Ha   1
    Department of Meteorology
    Naval Postgraduate School
    Monterey, California 93940

24. Dr. J. Holton   1
    Department of Atmospheric Sciences
    University of Washington
    Seattle, Washington 98105

25. Dr. B. J. Hoskins   1
    Department of Geophysics
    University of Reading
    Reading, United Kingdom

26. Dr. D. Houghton   1
    Department of Meteorology
    University of Wisconsin
    Madison, Wisconsin 53706

27. Dr. J. Wallace   1
    Department of Atmospheric Sciences
    University of Washington
    Seattle, Washington 98105

28. Dr. Carl Kreitzberg   1
    Department of Physics and Atmospheric Science
    Drexel University
    Philadelphia, Pennsylvania 19104

29. Dr. S. K. Kao   1
    Department of Meteorology
    University of Utah
    Salt Lake City, Utah 84112

30. Dr. A. Kasahara   1
    National Center for Atmospheric Research
    P. O. Box 3000
    Boulder, Colorado 80303

31. Dr. M. G. Wurtele   1
    Department of Meteorology
    University of California
    Los Angeles, California 90024

32. Dr. C. E. Leith   1
    National Center for Atmospheric Research
    P. O. Box 3000
    Boulder, Colorado 80303

33. Dr. J. M. Lewis   1
    Laboratory for Atmospheric Research
    University of Illinois
    Urbana, Illinois 61801

34. Dr. R. Madala   1
    Code 7750
    Naval Research Laboratories
    Washington, D. C. 20390

35. Dr. J. D. Mahlman   1
    Geophysical Fluid Dynamics Laboratory
    Princeton University
    Princeton, New Jersey 08540

36. Meteorology Library, Code 63   1
    Naval Postgraduate School
    Monterey, California 93940

37. National Center for Atmospheric Research   1
    Box 1470
    Boulder, Colorado 80302

38. Department of Oceanography, Code 68   1
    Naval Postgraduate School
    Monterey, California 93940

39. Office of Naval Research   1
    Department of the Navy
    Washington, D. C. 20360

40. Dr. Y. Ogura   1
    Laboratory for Atmospheric Research
    University of Illinois
    Urbana, Illinois 61801

41. Dr. I. Orlanski   1
    Geophysical Fluid Dynamics Laboratory
    Princeton University
    Princeton, New Jersey 08540

42. Prof. N. A. Phillips   1
    National Meteorological Center/NOAA
    World Weather Building
    Washington, D. C. 20233

43. Dr. S. Piacsek   1
    Code 7750
    Naval Research Laboratory
    Washington, D. C. 20390

44. Dr. J. Smagorinsky, Director   1
    Geophysical Fluid Dynamics Laboratory
    Princeton University
    Princeton, New Jersey 08540

45. Dr. T. Rosmond   2
    Naval Environmental Prediction Research Facility
    Monterey, California 93940

46. Dr. R. Pielke   1
    P. O. Drawer 5508
    Charlottesville, Virginia 22903

47. Dr. Chester Newton   1
    National Center for Atmospheric Research
    P. O. Box 3000
    Boulder, Colorado 80303

48. Dr. Harry Orville   1
    Institute of Atmospheric Science
    South Dakota School of Mines & Technology
    Rapid City, South Dakota 57701

49. Professor Yoshi K. Sasaki   1
    Department of Meteorology
    University of Oklahoma
    Norman, Oklahoma 73019

50. Mr. Murray Schefer   1
    Naval Air Systems Command 370C
    Washington, D. C. 20361

51. Dr. A. Wiin-Nielsen   1
    European Centre for Medium Range
    Weather Forecasts
    Fitzwilliam House, Skimped Hill
    Bracknell-Berks U.K.

52. Dr. Donald Johnson   1
    Space Science and Engineering Center
    University of Wisconsin
    1225 West Dayton Street
    Madison, Wisconsin 53706

53. Prof. T. Krishnamurti   1
    Florida State University
    Department of Meteorology
    Tallahassee, Florida 32306

54. Dr. Y. Kurihara   1
    Geophysical Fluid Dynamics Laboratory/NOAA
    Princeton University
    Princeton, New Jersey 08540

55. Dr. L. Leslie   1
    Australia Meteorology Research Centre
    P.O. Box 5089AA
    Melbourne, Victoria 3001
    Australia

56. Dr. A. Robert   1
    Centre Meteorologique Canadienne
    2121 Voie De Service Nord, Suite 100
    Route Trans Canada
    Dorval, Quebec-Canada H9P 1J3

57. Dr. L. Bengtsson   1
    European Centre for Medium Range
    Weather Forecasts
    Fitzwilliam House, Skimped Hill
    Bracknell, Berks U.K.

58. Mr. F. Bushby   1
    Meteorological Office
    London Road
    Bracknell, Berks, U.K.

59. Dr. J. Egger   1
    Meteorologisches Institut
    Der Universitat Munchen
    Theresienstrasse 37
    D8000 Munchen 2, F.R.G.

60. Dr. J. Hovermale   1
    National Meteorological Center/NWS
    NOAA World Weather Building
    Washington, D. C. 20233

61. Edward H. Barker   1
    Naval Environmental Prediction Research Facility
    Monterey, California 93940

62. Terry Tarbell   1
    Department of Meteorology
    The Pennsylvania State University
    503 Walker Building
    University Park, Pennsylvania 16802

63. Dr. Thomas T. Warner   1
    Department of Meteorology
    The Pennsylvania State University
    503 Walker Building
    University Park, Pennsylvania 16802

64. Daniel Keyser   20
    Department of Meteorology
    The Pennsylvania State University
    503 Walker Building
    University Park, Pennsylvania 16802

70

65. Dr. Richard A. Anthes   1
    Department of Meteorology
    The Pennsylvania State University
    503 Walker Building
    University Park, Pennsylvania 16802

66. Richard M. Hodur   1
    Naval Environmental Prediction Research Facility
    Monterey, California 93940

67. Dr. Donald J. Perkey   1
    National Center for Atmospheric Research
    P. O. Box 3000
    Boulder, Colorado 80307

68. Dr. James E. Hoke   1
    11812 South 31st Street
    Omaha, Nebraska 68123

69. Dr. Nelson L. Seaman   1
    Department of Atmospheric Science
    P. O. Box 3038
    University of Wyoming
    Laramie, Wyoming 82071

70. Patrick C. Gallacher   1
    Department of Meteorology, Code 63Ga
    Naval Postgraduate School
    Monterey, California 93940

71. Dr. Francis Binkowski   2
    Research Triangle Park
    Meteorology Division
    North Carolina 27709

72. Dr. Chandrakant M. Bhumralkar   1
    Stanford Research Institute
    333 Ravenswood Avenue
    Menlo Park, California 94025

73. Dr. Robert F. Adler   1
    NASA, Goddard Space Flight Center
    Greenbelt, Maryland 20771

74. Dr. Simon Chang   1
    JAYCOR
    205 S. Whiting Street
    Alexandria, Virginia 22314

75. Dr. Rainer Bleck   1
    Department of Meteorology
    University of Miami Beach
    Coral Gables, Florida 33124

76. Dr. Alan McNab
     Department of Meteorology
     The Pennsylvania State University
     503 Walker Building
     University Park, Pennsylvania 16802

77. Dr. John Cahir
     Department of Meteorology
     The Pennsylvania State University
     503 Walker Building
     University Park, Pennsylvania 16802

78. Dr. John W. Diercks
     818 Arlene Avenue
     Papillion, Nebraska   68046

79. Dr. William Gray
     Department of Atmospheric Sciences
     Colorado State University
     Fort Collins, Colorado 80523

80. Dr. William Cotton
     Department of Atmospheric Sciences
     Colorado State University
     Fort Collins, Colorado 80523

81. Dr. Stanley L. Rosenthal
     National Hurricane and Exp. Lab.
     P. O. Box 248265
     Coral Gables, Florida 33124

1

1

1

1

1

2